Electrodeposition to reduce the impact of cracks on steel corrosion in concrete

Cement and Concrete Composites 174 (2026) 106801

Contents lists available at ScienceDirect

Cement and Concrete Composites

journal homepage: www.elsevier.com/locate/cemconcomp

Electrodeposition to reduce the impact of cracks on steel corrosion in concrete

Suraksha Sharma [a,*], Karla Hornbostel [a,b], Rob Polder [c], Samanta Robuschi [d], Karin Lundgren [d], Tobias Danner [e], Roy Johnsen [f], Mette Rica Geiker [a,d]

[a] Department of Structural Engineering, Norwegian University of Science and Technology, Trondheim, Norway
[b] Norwegian Public Roads Administration, Trondheim, Norway
[c] RPCP, Gouda, the Netherlands
[d] Division of Structural Engineering, Chalmers University of Technology, Göteborg, Sweden
[e] SINTEF Community, Department of Architecture, Building Materials and Construction, Trondheim, Norway
[f] Department of Mechanical and Industrial Engineering, Norwegian University of Science and Technology, Trondheim, Norway

ARTICLE INFO

Keywords:
Reinforced concrete
Corrosion
Initial cracks
Electrodeposition
Tensile cracks

ABSTRACT

Electrodeposition has been proposed as a method to promote mineral precipitation in cracked reinforced concrete, potentially limiting ingress of aggressive agents and delaying corrosion initiation. However, the extent to which electrodeposition-induced crack filling improves corrosion resistance under marine exposure, and the influence of electrolyte composition on the effectiveness and mechanism of electrodeposition, remains overlooked.

This study investigated deposition behaviour of electrodeposition in either artificial seawater or Ca-Mg nitrate solution and evaluated corrosion performance of electrodeposition-treated (2x3) and non-electrodeposition-treated (references, 2x2) specimens during artificial seawater exposure.

Reinforced concrete cylinders containing tensile-induced transverse cracks underwent three-month electrodeposition treatment, followed by a three-month artificial seawater exposure. Crack filling and deposition patterns were examined using X-ray computed tomography (XCT), optical microscopy, and μXRF elemental mapping, while corrosion behaviour was assessed through half-cell potential monitoring and post-exposure CT. Analytical interpretation was further used to interpret observed electrodeposition behaviour.

A difference in Ca^{2+} and Mg^{2+} ion concentrations between the Ca-Mg nitrate solution and artificial seawater results in different crack-filling behaviour. Electrodeposition in Ca-Mg nitrate solution resulted in extensive internal crack filling reaching the steel-concrete interface, independent of crack geometry and width (maximum surface crack width 0.75 mm), and no corrosion was observed. In contrast, electrodeposition treatment in artificial seawater resulted in deposits primarily near the crack mouth and an influence of crack geometry. In these specimens, corrosion was prevented in two specimens and reduced in the third. The findings demonstrate that electrodeposition can delay corrosion initiation in cracked concrete when sufficient internal crack filling is achieved.

1. Introduction

Cracks may act as preferential pathways for chloride ingress in marine-exposed concrete [1–3], and increase the risk of corrosion initiation by altering the stability of the passive film [2,4]. To mitigate reinforcement corrosion, a range of repair and protection strategies is available, including conventional patch repair, surface treatments [5,6], electrochemical chloride extraction, and cathodic prevention or protection [7]. Among these, approaches based on electrodeposition (ED) of minerals have emerged as an alternative concept [8]. However, the mechanisms and crack filling efficiency of ED, as well as its effectiveness in terms of improved performance as reduction of chloride ingress, and limitation of corrosion initiation at cracks, remain comparatively underexplored, particularly for cracked members in marine exposure [8].

Danner et al. [8] described ED treatment as a crack-filling process in

* Corresponding author.
E-mail address: suraksha.sharma@ntnu.no (S. Sharma).

https://doi.org/10.1016/j.cemconcomp.2026.106801
Received 7 April 2026; Received in revised form 10 June 2026; Accepted 11 August 2026
Available online 12 August 2026

which an applied electrical field drives positive ionic species, predominantly Mg^{2+} and Ca^{2+}, from the surrounding electrolyte into cracks and interconnected interfacial voids, where they precipitate as brucite ($Mg(OH)_2$), calcium carbonate ($CaCO_3$), portlandite ($Ca(OH)_2$), and related mineral phases; at the same time the electrical field induces the outward transport of negative ions as hydroxyl and chloride. The ED accelerates mineral deposition, which progressively fills the crack, potentially reducing permeability and limiting the ingress of chlorides and other aggressive agents, thereby enhancing the structure's durability.

The earliest application of ED for protection originates from the mineral accretion concept proposed by W. Hilbertz (1981 and 1984) [9,10] in which an impressed current in seawater precipitates Ca-Mg minerals onto a cathode steel surface. This concept was later adapted to crack repair in reinforced concrete, as demonstrated by Ryu and Otsuki [11], who reported crack closure in chloride-damaged reinforced concrete beams by electrodeposition of ZnO from a $ZnSO_4$ electrolyte under constant current. It was subsequently developed further through more controlled crack-repair strategies for reinforced concrete, as demonstrated by Nishida et al. [12] and Chu et al. [13,14]. Nishida et al. [12] investigated the influence of repair conditions, including the external solution and external electrode, for reinforced concrete repair, while Chu et al. [13,14] studied ED in Mg- and Zn-based electrolytes containing sulphates, under direct current or pulsed current. More recently, Shirole et al. [15] showed that periodically reversed polarity can produce more uniform electrodeposition and improve concrete densification, strength, and permeability reduction compared with fixed-polarity current. Further, complementary modeling studies, summarised by Qian et al. [16] and supported by Chen et al. [17], clarified ion-transport behaviour in different electrolytes. Long-term field evidence from Danner et al. [8] showed that the presence of Mg and Ca in the marine environment can promote precipitation in cracks, gradually filling cracks over decades during the application of cathodic protection. Chen et al. [17] also compiled experimental parameters across Mg- and Zn-based ED systems and further investigated an ettringite-forming Ca-Al electrolyte system, which enabled rapid filling of 0.5 mm-wide cracks (depth ≈2-15 mm) and substantially reduced permeability. Collectively, these works establish ED as an alternative option for crack filling in concrete in aqueous environments while simultaneously revealing limitations in the existing knowledge base as follows:

- Electrolyte composition and applicability in marine exposure: most of the ED treatment studies used electrolytes with few ions (e.g., solutions containing $MgCl_2$, $MgSO_4$, $ZnSO_4$, Ca-Al, $Mg(NO_3)_2$, $Ca(OH)_2$) [13–15,17–19]. Marine exposure inevitably involves seawater containing a variety of ions. Accordingly, the relative effectiveness of ED treatment in seawater compared with other electrolytes remains underexplored. In the present study, a 0.5 M Ca-$Mg(NO_3)_2$ solution was selected as a benchmark electrolyte because it provides high concentrations of Ca^{2+} and Mg^{2+} ions relevant for ED precipitation. $Mg(NO_3)_2$ electrolyte has also been used in previous ED studies for crack repair in reinforced concrete [20,21]. The nitrate anion was used to introduce cations without adding chloride or sulphate ions, thereby avoiding additional chloride- or sulphate-related effects.
- Crack geometry: most ED studies rely on simple, idealised crack geometries, typically straight, one crack per specimen, as in Refs. [13,14,17], and the systems summarised in Ref. [16]. These studies predominantly report surface crack closure, crack filling, or reductions in permeability, but they provide limited information on deposit propagation under varying crack configurations [17]. Furthermore, cracks interconnected with macroscopic voids at the steel–concrete interface (SCI) have not been studied.
- From crack filling to limiting corrosion initiation: while many investigations focus on crack filling or permeability reduction [13,14,17], the relationship between crack filling and reinforcement corrosion has not been addressed. Thus, the effectiveness of ED in limiting the initiation and propagation of corrosion at cracks remains to be studied.

The present study is structured around three research questions: (1) Where does the deposition take place, and up to which crack width and depth can ED deposits fill cracks? (2) Is ED treatment in seawater equally effective as ED treatment in a 0.5 M Ca-$Mg(NO_3)_2$ solution? and (3) How effective is ED in limiting corrosion initiation at cracks?

Reinforced concrete specimens with a single centrally embedded rebar were cracked in tension to produce transverse cracks (surface crack widths up to a maximum of ~1.4 mm). Before corrosion testing in artificial seawater (ASW), reference specimens were either treated by immersion in a Ca-$Mg(NO_3)_2$ solution (CMN) without current or left without pre-treatment, whereas the remaining specimens were treated with ED in either ASW or CMN. After their respective treatments, all specimens were immersed in ASW for three months. Half-cell potentials were monitored during both the treatment phase and subsequent ASW exposure. Crack-filling and deposition patterns were characterised using CT scanning, μXRF elemental mapping, and optical microscopy of impregnated sections. Solution pH and conductivity were measured to determine possible changes in the electrochemical environment.

2. Experimental investigations

The experimental study was designed to investigate reinforcement corrosion in cracked concrete after ED treatment. The study is part of a collaborative project between Chalmers University of Technology (Chalmers) and the Norwegian University of Science and Technology, Trondheim (NTNU). To ensure comparability between the corrosion studies, all specimens were cast and cracked at Chalmers and subsequently transported to NTNU for further investigation.

2.1. Materials

Reinforced concrete cylinders (ϕ 44 mm, length 420 mm) were cast and cracked. Ordinary reinforcing steel bars (ϕ 8 mm, ribbed, (K 500C, Gothia Armering SS212540:2014, CERT: A3/045) in as-received state were inserted in the moulds (oiled cylindrical PE pipes) and centred by fixing protruding reinforcement on both ends. The concrete composition is provided in Table 1. The concrete was prepared in two batches. Dry aggregates were first mixed, cement was added, followed by the addition of water and superplasticizer.

The moulds were kept vertical when casting. The concrete was poured into the moulds in three layers. Each layer was compacted by tamping, followed by vibration of the mould surface with a poker vibrator until no further air voids appeared on the surface. The vibration of the last layer created a smooth surface with a thin film of bleed water on the top. The moulds were sealed with plastic locks, placed horizontally, and left in laboratory conditions for 3 days. Then the cylinders were demoulded and wrapped in a thin plastic film, followed by an outer layer of thicker plastic wrap, to reduce moisture loss from the specimens before and after subsequent preparation.

The specimens were cracked in tension after 5 to 7 days of curing. All specimens were cracked at a similar early age using the same procedure. Cracks were induced by applying tensile force to the reinforcement to attain one major crack. The specimens were initially loaded until the reinforcement bar reached its yielding point. At this point, several small cracks had formed along the length of the specimens. The specimens were then unloaded and reloaded up to yielding. At this point, the displacement was manually increased in 0.1 mm increments until crack localisation occurred in a single dominant crack, after which the load was removed. Except for one specimen, this resulted in one single crack, which stayed open after unloading by the plastic deformation of the reinforcement. Specimen, CMN-ED-II, had two dominant cracks. The remaining cracks closed and were very small after unloading.

After completing the tensile test, the cracked cylinders were again

Table 1
Concrete recipe, D_{max} = 8 mm. Admixtures in percent of cement weight. D_{max} denotes the maximum aggregate size.

Binder	Cement (kg/m^3)	Water (kg/m^3)	Coarse Aggregates (kg/m^3)	Fine Aggregates (kg/m^3)	Super-plasticizer (Glenium) (%)	Retarder (%)	W/C ratio
CEM II/A-LL 42.5R	387	210	948	740	0.53	0.3	0.55

wrapped in plastic and shipped to NTNU. Upon arrival, the cylinders were prepared for further testing by removing the protruding bar and approximately 50 mm of concrete from the bottom end using a concrete sawing machine (final length of concrete cylinders approximately 370 mm). Following this, wires were soldered to the still present protruding reinforcement bars, except for two cylinders, where wires were connected using screws. They were then wrapped in layers of thin and thick plastic wrap and stored in the lab (T ≈ 22 °C). At 42 days of age, the specimens were further prepared. Upon unwrapping, all specimens exhibited clean surfaces at the cut section, with no signs of corrosion. To prevent crevice corrosion during later exposure, a three-layer protective system was applied: two layers of cementitious (Redisit) coating (up to 10 mm from the cut bottom end) with a 2 h interval, followed by 24 h of curing at 100% relative humidity in a climate room (T ≈ 22 °C) and 12 h of drying at laboratory conditions, and then a final 8 mm layer of epoxy coating as presented in Appendix (Fig. A1). The protruding bars left at the top section were cleaned with isopropanol and coated similarly to prevent corrosion. The epoxy coating was allowed to dry for 24 h, after which the specimens were wrapped again and stored for 52 days.

2.2. Experimental design, treatment, and subsequent exposure

The experimental setup consisted of 10 reinforced concrete specimens, divided into four groups according to the treatment applied before exposure to corrosive conditions (ASW immersion), see Table 2 and Fig. 1. Individual specimens were designated by the group ID followed by a Roman numeral indicating the specimen number within the group (e.g., 0-I denotes the first specimen in Group 0). Specimens with surface crack widths up to 0.7 mm were included in all groups. Three types of treatment were employed: i) no treatment, ii) immersion in a solution of Ca $(NO_3)_2$ and Mg $(NO_3)_2$ (1:1) (CMN), and iii) ED treatment, where an external current was applied to induce ED during immersion in either CMN or ASW. After the respective treatments, the specimens were exposed to ASW (corrosive exposure) for approximately three months.

Detailed descriptions of ED treatment and ASW immersion are provided in Sections 2.3.2 and 2.3.3, respectively. Following the respective treatment and subsequent ASW exposure phases, all groups underwent a sequence of characterisation and post-exposure analyses, including visual inspection, computed tomography (CT), optical microscopy, and μX-ray fluorescence (μXRF) mapping, as described in Section 2.3. An overview of investigations performed on the specimens and solutions is provided in Table 3.

The solutions used were prepared according to the composition outlined in Table 4. Artificial seawater was selected instead of natural seawater to ensure experimental reproducibility; the composition used by Ref. [22] was used.

The experiment was conducted in a well-ventilated laboratory to mitigate the risk of undesirable buildup of hydrogen and chlorine. The container lid was left open to prevent gas accumulation, resulting in solution evaporation, which was compensated for by adding distilled water at three-day intervals to maintain the solution volume. Conductivity and pH measurements of the solutions were recorded both before and after the treatment phase.

Table 2
Experimental matrix listing the number of specimens and the corresponding treatments prior to corrosive exposure in artificial seawater.

Specimens		Treatment				Corrosive exposure
Group ID	No.	Solution	Current (A/m^2)	Duration (month)	Total charge (C)	Solution
0	2	-	-	-	-	ASW
CMN	2	CMN	0	3	-	ASW
CMN-ED	3	CMN	1	3	2.1×10^5	ASW
ASW-ED	3	ASW	1	3	2.1×10^5	ASW

2.3. Experimental methods

2.3.1. Visual inspection and surface crack width measurement

The specimens were visually inspected, and surface crack widths were measured prior to exposure using a crack width ruler with a minimum measurement of 0.05 mm and a maximum of 10.0 mm. To ensure consistency, the measurements were conducted by a single individual (the first author), as crack width readings can vary between observers.

2.3.2. Treatment by electrodeposition

The schematic experimental setup for ED treatment is illustrated in Fig. 2. The container volume was 28 L. For ED, MMO-coated titanium (330 mm × 200 mm) mesh was used as anode. A bare titanium strip, protruding a minimum of 200 mm above the solution, was attached to the titanium anodes to prevent galvanic corrosion of contact clips. A CAMUR cathodic protection setup was used. The treatment was designed to apply a current density of 1 A/m^2 to a rebar surface area of 0.027 m^2, corresponding to a target current of 0.027 A. The test was initially planned for 90 days, with the aim of delivering a total charge of 2.1×10^5 C. To maintain the current at the predetermined level, the voltage was adjusted periodically, and the current and voltage were recorded automatically every 6 h. As the three specimens in each group (CMN-ED and ASW-ED) were connected to a single power source, the current to individual specimens was not monitored separately. However, because the applied current fluctuated during the experiment, the actual current was 0.025 ± 0.005 A. To achieve the cumulative charge of 2.1×10^5 C, the CMN-ED specimens were exposed in CMN for 100 days, whereas the ASW-ED specimens were exposed in ASW for 95 days.

Half-cell potentials were monitored using MnO_2 (ERE20) reference electrodes placed in the solution near the specimens, connected to an electrical potential measuring device (IIP node) integrated into the CAMUR monitoring system. The specimens were immersed in their respective solutions for four days to stabilise the potentials before the current was impressed. For reporting purposes, the measured potentials are expressed versus CSE.

Fig. 3 illustrates the possible reactions that occur during electrodeposition using either ASW or CMN. In both solutions, reduction of water at the cathode produces a strong flow of hydroxyl ions that precipitates $Ca(OH)_2$ and $Mg(OH)_2$ within cracks if sufficient cations (Ca^{2+} and Mg^{2+}) are present. At the cathode, hydrogen evolution is predominant over oxygen reduction as it has been documented for high current densities [7]. The anodic region becomes acidic due to water oxidation (predominant over hydroxyl oxidation) in both CMN and ASW; in ASW, the presence of Cl^- generates Cl_2 gas. The different anodic reactions, shown together in Fig. 3, highlight the differences in chemical gradients and reaction products that develop during polarisation in the two electrolytes.

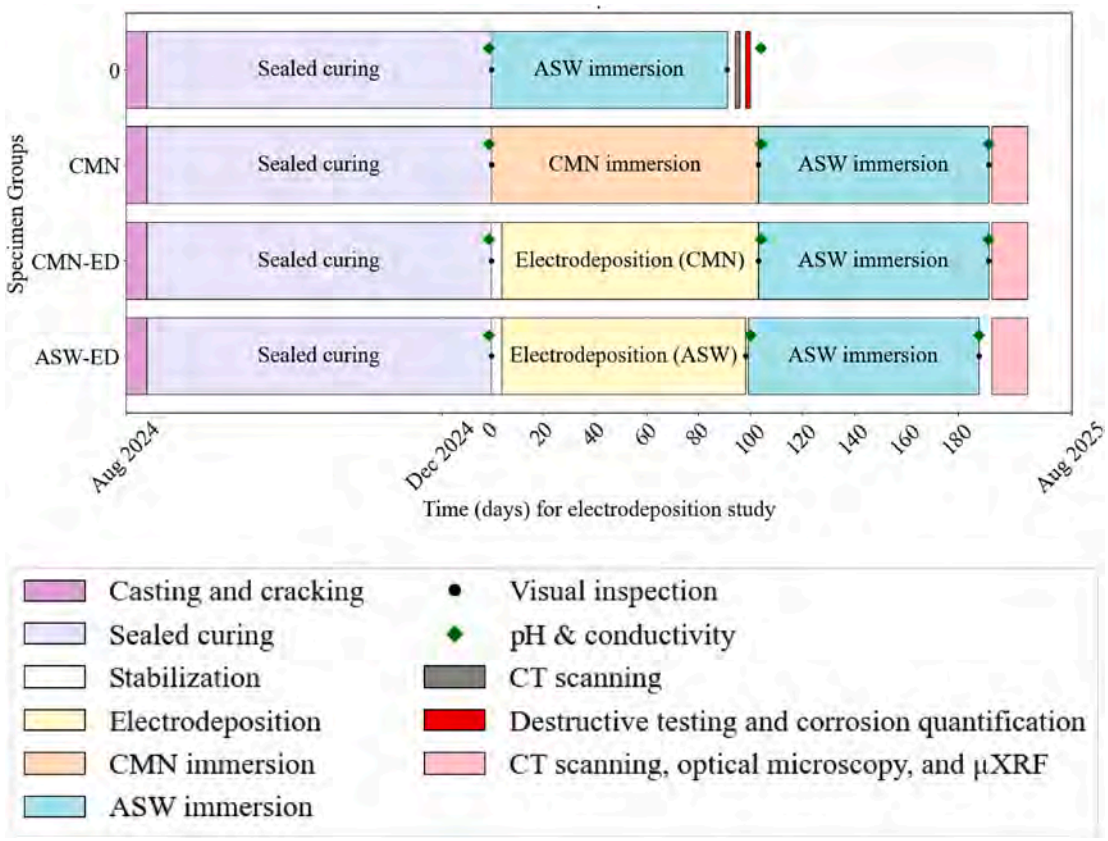

Fig. 1. Timeline of experimental work performed on the specimens.

Table 3
Overview of investigations on exposed specimens and solutions.

Specimens	Visual inspection	CT scanning	Optical microscopy	μXRF	pH and conductivity
0	x	x	-	-	-
CMN	x	x	-	-	-
CMN-ED	x	x	x (CMN-ED-I)	x	-
ASW-ED	x	x	x (ASW-ED-I)	x	-
Solutions	-	-	-	-	x

Table 4
Composition of solutions, conductivity, and pH.

CMN (0.5M of each compound)					
Reagents		$Ca(NO_3)_2{\cdot}4H_2O$			$Mg(NO_3)_2{\cdot}6H_2O$
Quantity (g/L)		118.08			128.21
pH		5.90			
Conductivity (mS/cm)		122.80			
ASW [22]					
Reagents	NaCl	KCl	$CaCl_2$	$MgCl_2{\cdot}6H_2O$	$MgSO_4{\cdot}7H_2O$
Quantity (g/L)	26.29	0.74	0.99	6.09	3.94
pH	6.10				
Conductivity (mS/cm)	51.10				

2.3.3. Corrosion monitoring in artificial seawater

The corrosion behaviour of all specimens was assessed through half-cell potential measurements to evaluate their electrochemical behaviour during exposure to ASW. To ensure sufficient oxygen availability, the solution was aerated with air using one air pump (EIHM Air 100) for every two containers. The experimental setup is shown in Fig. 4. For specimens in groups 0 and CMN (see Table 2), stainless-steel cathodes coupled with zero-resistance ammeters (ZRAs) were connected during the first two months with the intention of recording corrosion (macro-cell) currents. However, it was later discovered that the ZRAs had been nonfunctional throughout this period and that the cathodes had never been connected to the rebars (intended anodes). After this finding, monitoring continued using only potential measurements, and the stainless-steel cathode was removed from the system. Any short-term fluctuations observed around the time of ZRA removal should be interpreted with caution, as they may not reflect actual electrochemical behaviour (see Section 3.1). The potentials were monitored similarly as discussed in Section 2.3.2.

During exposure to ASW, specimen CMN-ED-I exhibited corrosion on the reinforcing bar protruding above the solution. To eliminate possible interference with test results, the corroded area was cleaned with a steel wire brush, coated with a cementitious layer, and then sealed with a rubber coating and a hydrophobic corrosion-inhibiting grease. The same protective procedure was applied to all specimens to prevent corrosion and maintain consistency.

2.3.4. Visual inspection of specimens

Prior to immersion, all specimens were visually inspected with the naked eye, and surface crack widths were measured as described in Section 2.3.1.

Visual inspection was also performed on specimens after approximately three months of treatment and after ASW immersion.

2.3.5. X-ray computed tomography (XCT)

X-ray-based imaging techniques have, in recent years, gained popularity as a non-destructive method for observing and quantifying corrosion in reinforced concrete specimens [23–25]. X-ray computed tomography (XCT) was conducted on all specimens to obtain volumetric data along their entire length, except for those in Group 0, for which only regions adjacent to the surface cracks were scanned. However,

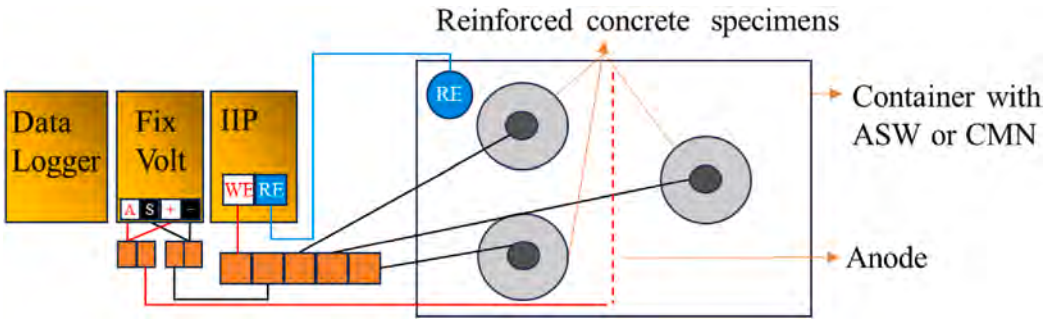

Fig. 2. Schematic diagram for electrodeposition treatment setup for specimens submerged in solutions, RE: reference electrode, WE: working electrode. The control and measuring devices are shown in yellow; IIP: electrical potential measuring device. (For interpretation of the references to colour in this figure legend, the reader is referred to the Web version of this article.)

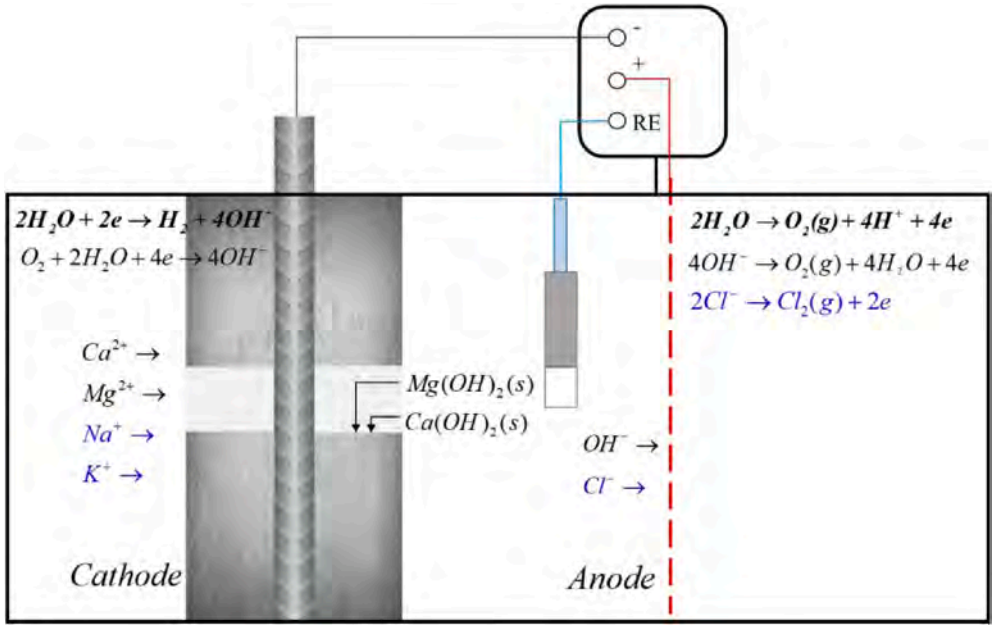

Fig. 3. Schematic of probable transport of ions, electrochemical reactions, and precipitation taking place during electrodeposition in artificial seawater or Ca-Mg nitrate solution; phenomena taking place only in artificial seawater are indicated in blue. (For interpretation of the references to colour in this figure legend, the reader is referred to the Web version of this article.)

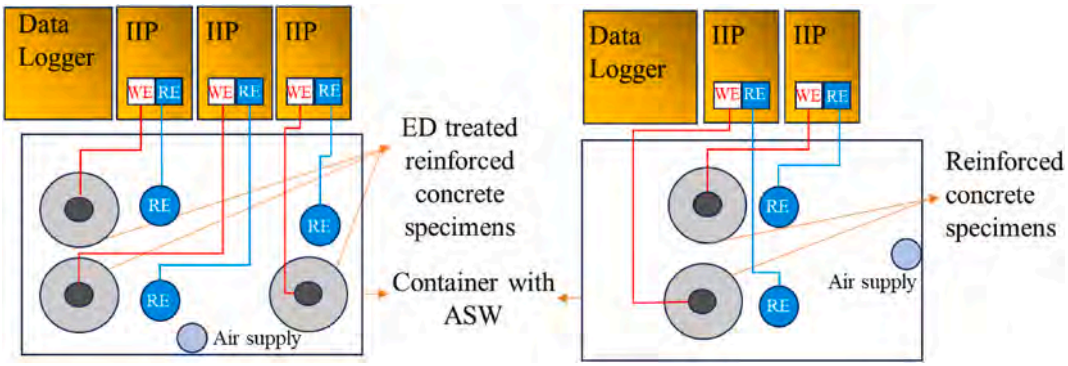

Fig. 4. Schematic diagram for monitoring of specimens during corrosive exposure (left: ED-treated specimens, right: reference specimens). RE: reference electrode, WE: working electrode. The measuring devices are shown in yellow, IIP: potential measuring device. (For interpretation of the references to colour in this figure legend, the reader is referred to the Web version of this article.)

these specimens were also opened and visually examined after scanning. Scanning was performed at the 4D Imaging Lab at Lund University, using an EasyTom150 micro-CT (RX Solutions, Chavanod, France). Specimens were mounted vertically and centred on the rotation axis. Eleven overlapping scans were acquired to capture the full specimen length at 150 kV and 75 W, using 0.35 mm Cu and 0.3 mm steel filters.

Each sub-scan comprised 2944 projections over 360° with three-frame averaging at 4 fps (1840 × 1456 pixels). Reconstructions with RXSolutions XAct software yielded 3D volumes with 26.5 μm isotropic voxels, generated in two overlapping subvolumes due to RAM limitations.

The reconstructed volumetric datasets obtained from X-ray CT scanning were analysed using Dragonfly 3D (version 2024.1.0.1627; Object Research Systems (ORS) Inc., Montreal, Canada; academic license; Windows) [26]. The datasets were analysed using grey-scale intensity values. All specimens were scanned using the same CT instrument under identical scanning conditions, allowing the thresholding procedure to be applied consistently across the dataset. For the 2D reconstructed images, a grey-value threshold range of 5000 to 42000 was applied unless stated otherwise in the corresponding figure. For 3D visualisation, the rebar phase was segmented using a grey-scale intensity-based thresholding approach, with the threshold set to isolate the rebar while excluding the surrounding concrete matrix. The threshold values adopted in each case are reported in the corresponding figures. The CT-based corrosion observations were further checked by destructive evaluation of the reference specimens in Group 0 after CT scanning.

2.3.6. Sectioning of specimens

2.3.6.1. Impregnation of specimens. To maintain structural integrity and prevent disturbing existing cracks and possible precipitation within them, all specimens were epoxy-impregnated before cutting for optical microscopy and subsequent μXRF. After CT scanning, both ED-treated and CMN-immersed specimens were brought to the laboratories of PELCON ApS, Denmark. Initial drying was performed outdoors, sheltered from the sun and rain, for approximately 36 h. Subsequently, the specimens were oven-dried at 35 °C for a few hours. Before impregnation, the rebar ends were trimmed with a bolt cutter due to the length of the protruding reinforcement bars exceeding the height of the available vacuum chamber. All specimens were then subjected to vacuum impregnation with a low-viscosity, fluorescent-dyed epoxy resin, following PELCON's standardised procedure, which comprises vacuum evacuation and resin infiltration.

2.3.6.2. Subsectioning of impregnated cracked regions. A 40 mm segment was cut at the locations of the widest surface cracks of specimens CMN-ED-I and ASW-ED-I using a water-cooled diamond saw. Immediately after cutting, the surfaces were patted dry and sprayed with alcohol to displace water for minimizing the dissolution of salts and other precipitates. The cut segments were oven-dried at 35 °C for a few hours to remove residual solvent.

From the anode-facing region during ED treatment in both specimens (CMN-ED-I and ASW-ED-I), a roughly ~45° wedge-shaped subsections were extracted for optical microscopy. A kerosene-cooled diamond saw was used to prevent dissolution of water-soluble precipitates and thus preserve the microstructure. The subsections were briefly oven-dried at 35 °C and subsequently packed in a zip-lock bag with silica gel.

From the specimens (CMN-ED I and II, and ASW-ED I, II, and III), sawing (using water cooling) was performed to cut wedge-shaped subsections for elemental mapping using the μXRF. Some specimens were cut into two slices, depending on the number of cracks chosen for μXRF.

2.3.7. Optical microscopy

To allow for additional investigation of possible electrodeposition in large cracks (~0.7 mm), two of the specimens, which underwent ED treatment (CMN-ED-I and ASW-ED-I) and subsequent impregnation, were analysed under optical microscopy.

2.3.8. μXRF

Sections from all ED-treated specimens (CMN-ED-I and II, and ASW-ED-I, II, and III) were further analysed using μXRF to evaluate the extent and elemental distribution of deposits. Elemental mapping was carried out at RISE, Sweden, using an M4 Tornado instrument (Bruker) to determine the elemental content of Mg, Ca, Cl, and other selected elements. The settings for data collection were 50 kV voltage, 600 μA current, pixel distance 30 μm, 20 μm pixel size, and 2 ms/pixel acquisition time. μXRF was performed in two runs (1 of each cut side) in one scan.

2.3.9. Quantification of reinforcement corrosion

Reinforcement corrosion of specimens in Group 0 was quantified through a combination of CT scanning and destructive testing. Destructive examination of the Group 0 reference specimens was used as a check for the CT-based corrosion assessment, and the other specimens were evaluated solely by CT scanning. For the specimens in the 0 group, the full-length reinforcement was carefully extracted from the concrete. Pitting corrosion was assessed by measuring the longitudinal extent of individual pits along the bar surface using a ruler.

3. Results

3.1. Visual appearance and surface crack widths

Surface imperfections, such as voids and visible cracks, were identified in the specimens. Specimens with larger crack widths were included in all groups (0, CMN, CMN-ED, and ASW-ED). The measured surface crack widths are provided in Fig. 5. It can be observed that the crack widths varied both between different specimens and within individual specimens.

3.2. Characterisation of specimens

In addition to surface observations from visual inspection, CT scans were employed to examine the internal condition of the specimens at the steel–concrete interface (SCI) after exposure. The CT scans enabled visualisation of crack continuity and internal features that were not accessible from surface inspection alone. Some cracks were straight through-cracks, whereas other cracks were observed to branch in proximity to the reinforcement. Each branch had a smaller crack width than the measured surface crack width. As summarised in Table 5, the CT data were also used to assess whether the largest surface-visible cracks were connected to interfacial macroscopic voids present at the SCI. Notably, neither of the specimens in Group 0 exhibited voids connected to the largest crack, whereas it was observed in most specimens from the other groups.

3.3. pH and conductivity of solutions

Before and after the treatment, pH and conductivity measurements were conducted on the solutions in which the specimens were immersed. The results are shown in Fig. 6. For the solutions without ED treatment, a slight increase in pH was observed compared to the initial values. In contrast, the solution of specimens exposed to ED treatment exhibited a significant decrease in pH. The conductivity showed a significant reduction for CMN of about 20%, both with and without ED treatment.

3.4. Deposits formed by electrodeposition in cracks

3.4.1. μXRF

The results from μXRF mapping of the two cut surfaces of the seven sections from the five ED-treated specimens having cracks larger than 0.1 mm are presented in Fig. 7. The figure clearly shows the presence of Mg (dark blue) within the cracks, confirming its incorporation into the ED deposits. Ca is distributed throughout the specimen as a main component of the cement paste, as indicated by the green colour; however, the localised cyan regions in the cracks demonstrated that Ca is also present in the ED deposits, though not as readily visible as Mg.

In the CMN-ED specimens, most cracks are filled in the internal

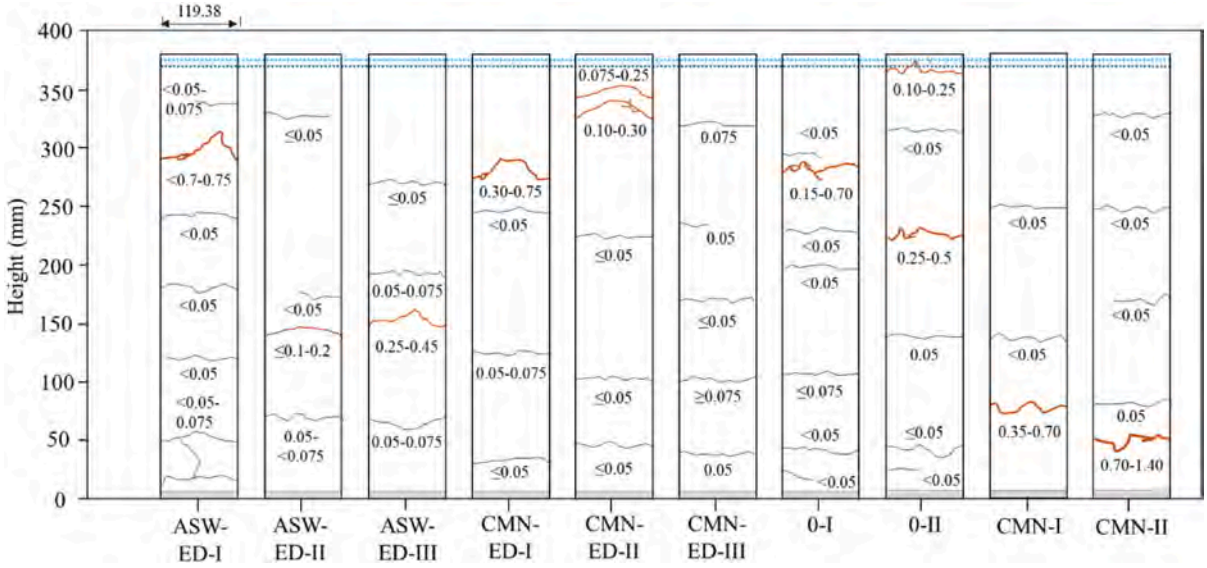

Fig. 5. Location of cracks at the full circumference and surface crack width in investigated specimens (brown ≥ 0.1 mm, grey <0.1 to 0.05 mm). All dimensions are in mm. The light and dark blue lines show the maximum and minimum solution levels. The grey area at the bottom represents the Redisit (cementitious) and epoxy coating. Measurements were taken before any treatments were applied to the specimens. (For interpretation of the references to colour in this figure legend, the reader is referred to the Web version of this article.)

Table 5
CT scan observations of interfacial voids and crack connectivity.

Specimen	Presence of interfacial macroscopic voids?	Connected to largest crack?
0-I	Yes	No
0-II	Yes	No
CMN-I	Yes	No
CMN-II	Yes	Yes
CMN-ED-I	Yes	Yes
CMN-ED-II	Yes	Yes
CMN-ED-III	Yes	No
ASW-ED-I	Yes	No
ASW-ED-II	Yes	Yes
ASW-ED-III	Yes	Yes

regions, whereas in some specimens, partial filling is observed closer to the surface; some fillings are also observed along parts of the SCI. In contrast, the ASW-ED specimens exhibit full deposition at the surface (crack mouth) but only partial or no filling towards the reinforcement.

3.4.2. *Imaging-based characterisation of deposits formed by electrodeposition*

All specimens were scanned using X-ray tomography. Moreover, optical microscopy images from specimens CMN-ED-I and ASW-ED-I were used to compare with CT scans and to verify the deposition pattern in the specimens. In each specimen, the largest cracks with crack widths greater than 0.1 mm were analysed by μXRF to assess the effectiveness of the ED treatment. The same cracks were examined using all characterisation techniques (CT scanning, μXRF, and optical microscopy); however, the exact cross-sectional slices analysed may differ between techniques. In CT scans, cement paste and electrodeposits could not be reliably separated by grey-value thresholding because of their similar densities. Therefore, CT was used to assess whether the continuity of the crack opening was interrupted, indicating filling of the crack space. This interpretation was supported by μXRF and optical microscopy, where available.

Fig. 8 depicts the μXRF, CT scanning, and optical microscopy findings regarding the nature of the crack fillings in the specimen CMN-ED-I. The specimen displays cracks fully filled with internal deposits. As shown in Fig. 8c, the optical microscopy reveals that the white deposits densely fill the crack. This trend is consistent with the corresponding μXRF (Mg elemental mapping) and CT scan results (Fig. 8a–b). It should be noted that Mg deposits (blue in Fig. 8a are distributed along the (imprint of the) steel bar, supposedly in bleeding zones or otherwise porous areas.

In contrast, the ASW-ED-I specimen, Fig. 9c, illustrates that the crack is sealed at the outer surface but exhibits limited deposition along its interior. The μXRF elemental maps (Fig. 9a) further confirm this, showing magnesium enrichment concentrated at the surface and partially extending from the exterior into the crack. However, in the case of CT scans, near the SCI, it was difficult to verify crack filling.

Table 6 presents the degree of crack filling for all ED-treated specimens at the largest crack, as evaluated by CT scanning, μXRF, and optical microscopy for different surface crack widths and crack regions. Deposition results were qualitatively classified into three categories: Full, Partial, and Empty. For CMN-ED specimens, filling was observed across most crack regions, including the SCI, whereas ASW-ED specimens showed partial or no filling in the middle and near-bar regions. Variations between techniques reflect differences in the regions assessed and in detectability. In the CT scans, cement paste and electrodeposits could not be distinguished because of their similar densities; filled crack regions were therefore interpreted as electrodeposits. However, in the CT scans of all specimens, it was difficult to verify crack filling near the SCI; this region was therefore termed difficult to characterise. The table provides a comparative overview of crack-filling characteristics across specimens (including scans 1 and 2, and the specimens cut using kerosene) and the investigation methods.

3.5. *Half-cell potentials*

In the present study, half-cell potential measurements were used to monitor the electrochemical condition of the reinforcement.

3.5.1. *Potentials in specimens without treatment*

Over a three-month exposure period in artificial seawater solution, specimens 0-I and 0-II were monitored, and the half-cell potential measurements are presented in Fig. 10. It can be observed from the graph that there is a rapid initial drop (−230 mV_{CSE} to −500 mV_{CSE}) in the potential in the first few days, indicating a gradual loss of oxygen in

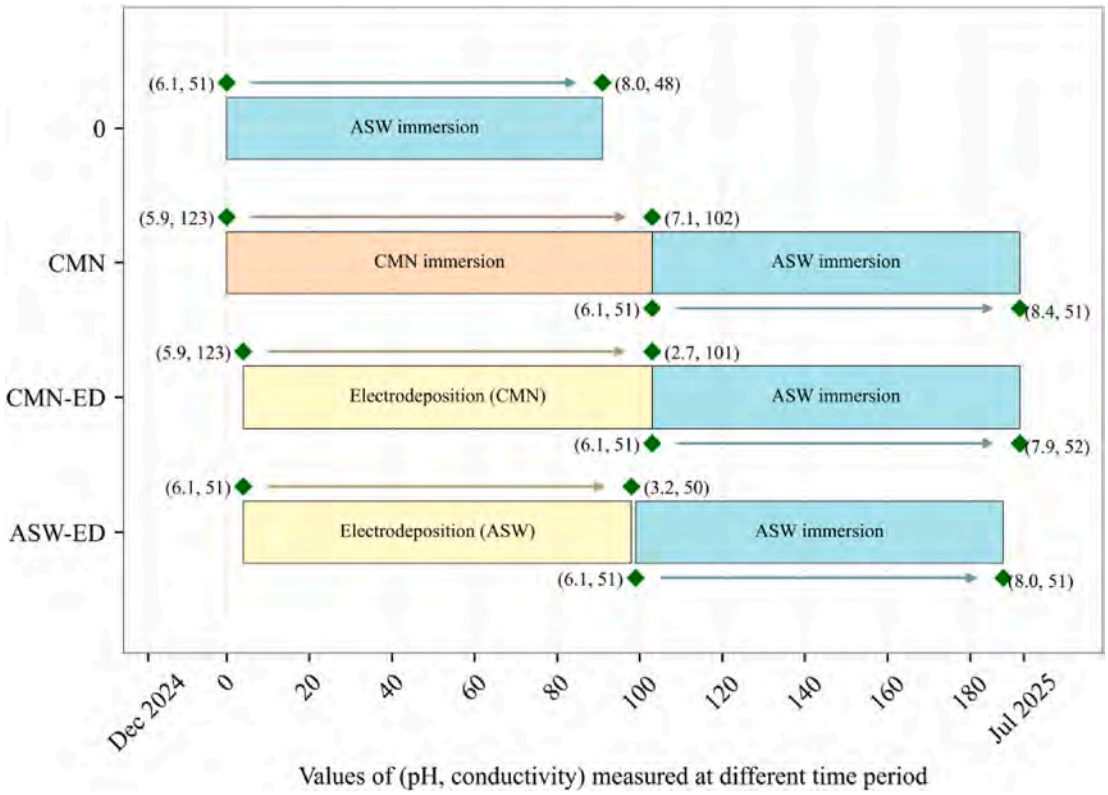

Fig. 6. Overview of pH and conductivity (mS/cm) of solutions measured at different stages of the investigation (pH, conductivity).

the specimens. Then it has gradually decreased from around −500 mV_{CSE} to −900 mV_{CSE} over the time frame, indicating initial depassivation and subsequently some level of active corrosion at the reinforcement in the crack location. The peaks observed after 54 days in both ASW (see Fig. 10) and CMN (see Fig. 11) immersed specimens were due to temporary contact between the nonfunctional cathode and the reinforcement (see Section 2). The resulting shift in potential is due to the formation of a mixed potential between the steel reinforcement and the external cathode during this brief connection. These peaks are artefacts and are not considered further.

3.5.2. Potentials in specimens with treatment

3.5.2.1. Immersed in Ca-Mg nitrate solution without current. During immersion in CMN, the trend of potentials of specimens, see Fig. 11, sharply declined in the beginning, probably due to solution penetration and less availability of oxygen in the specimens, but remained relatively stable without any further potential drops, with potentials around −400 mV_{CSE} to −450 mV_{CSE}.

Shortly after immersing in ASW, a drop in the potential was observed for both specimens. Specimen CMN-I stabilised after a few days, maintaining a relatively steady potential for three weeks (approx. 20 days), when a small second drop was observed to a level of −500 mV_{CSE}, indicating possible initiation of corrosion. Specimen CMN-II exhibited a larger decline to a level of −600 mV_{CSE}, indicative of corrosion initiation.

3.5.2.2. Ca-Mg nitrate solution with current. The potentials developed in the specimens during current application in the CMN (see Fig. 12) have returned from ON potentials to open-circuit potentials after immersion in the ASW on 100th day of ED treatment. Specimen CMN-ED-II exhibits a stable and relatively positive potential throughout the exposure to ASW, indicating passivation. On the other hand, specimens CMN-ED-I and CMN-ED-III exhibit a gradual decline in potential, indicating uncertainty about the onset of corrosion.

3.5.2.3. Artificial seawater with current. Fig. 13 shows a graph reporting the half-cell potentials of the specimens in ASW, both during treatment (ED) and during corrosive exposure (ASW immersion). The blue line (trace) indicates the ON potential during treatment, and the orange, green, and magenta traces indicate open circuit potentials during immersion in ASW after treatment. After treatment, the potentials stay very negative with specimen ASW-ED-I and ASW-ED-III, very stable throughout, ranging between −1070 and −1120 mV_{CSE}. However, specimen ASW-ED-II shows an increase from about −1100 to −850 mV_{CSE}.

3.6. Observation of corrosion at cracks

The corrosion behaviour of the reinforcement differed markedly between the treatment conditions. Corrosion was observed in all specimens without ED treatment and in one specimen treated with ED in artificial seawater (ASW-ED-I), whereas no corrosion was detected in CMN-ED specimens. Fig. 14 provides a schematic overview of the crack locations and the corresponding positions where corrosion was identified along the reinforcement bars.

The corrosion locations were determined from CT scans of the entire specimens. Due to the epoxy impregnation, destructive examination of most reinforcement bars was not feasible, and the corrosion assessment therefore relied primarily on CT scan observations. Destructive testing was only performed on specimens 0-I and 0-II, which validated the corrosion locations identified by the CT scans. In most specimens, corrosion was observed at the cross-section corresponding to the largest crack, and this location was therefore examined. In specimen 0-II, however, the second-largest crack was analysed, as corrosion was observed there. Fig. 15 shows the condition of the reinforcement at the cross-sections corresponding to the crack locations. Corrosion was localised on one side of the reinforcement in specimens 0-I and ASW-ED-

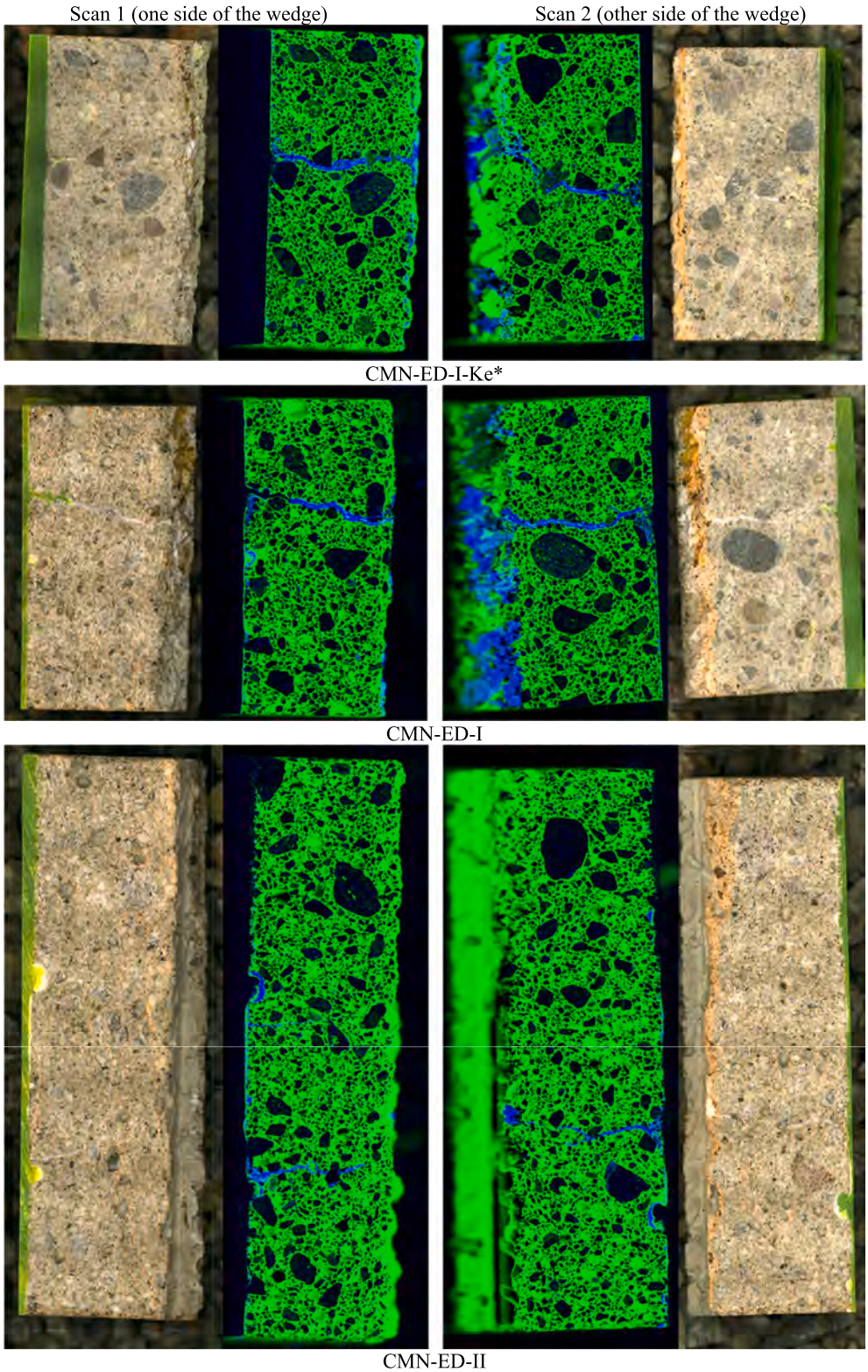

Fig. 7. μXRF scans of one side of the sections from the five ED-treated specimens having cracks larger than 0.1 mm. Order of sections (ASW-ED-I and CMN-ED-I appear twice as separate sections were cut with cooling by either kerosene (*Ke) or water). Left and right: Scans 1 and 2. The mosaic form of the specimens and their elemental mapping for Mg and Ca on the ED specimens. Rebar imprints appear on the right side in the specimens on the left, and on the left side in the specimens on the right.

I. In specimen 0-II, corrosion was observed on both sides of the reinforcement at the crack location, whereas in the CMN specimens, it extended around the full circumference of the reinforcement.

3.6.1. Corrosion in specimens without treatment

After approximately three months of exposure in ASW, specimens 0-I and 0-II exhibited rust-coloured spots on the concrete surface around

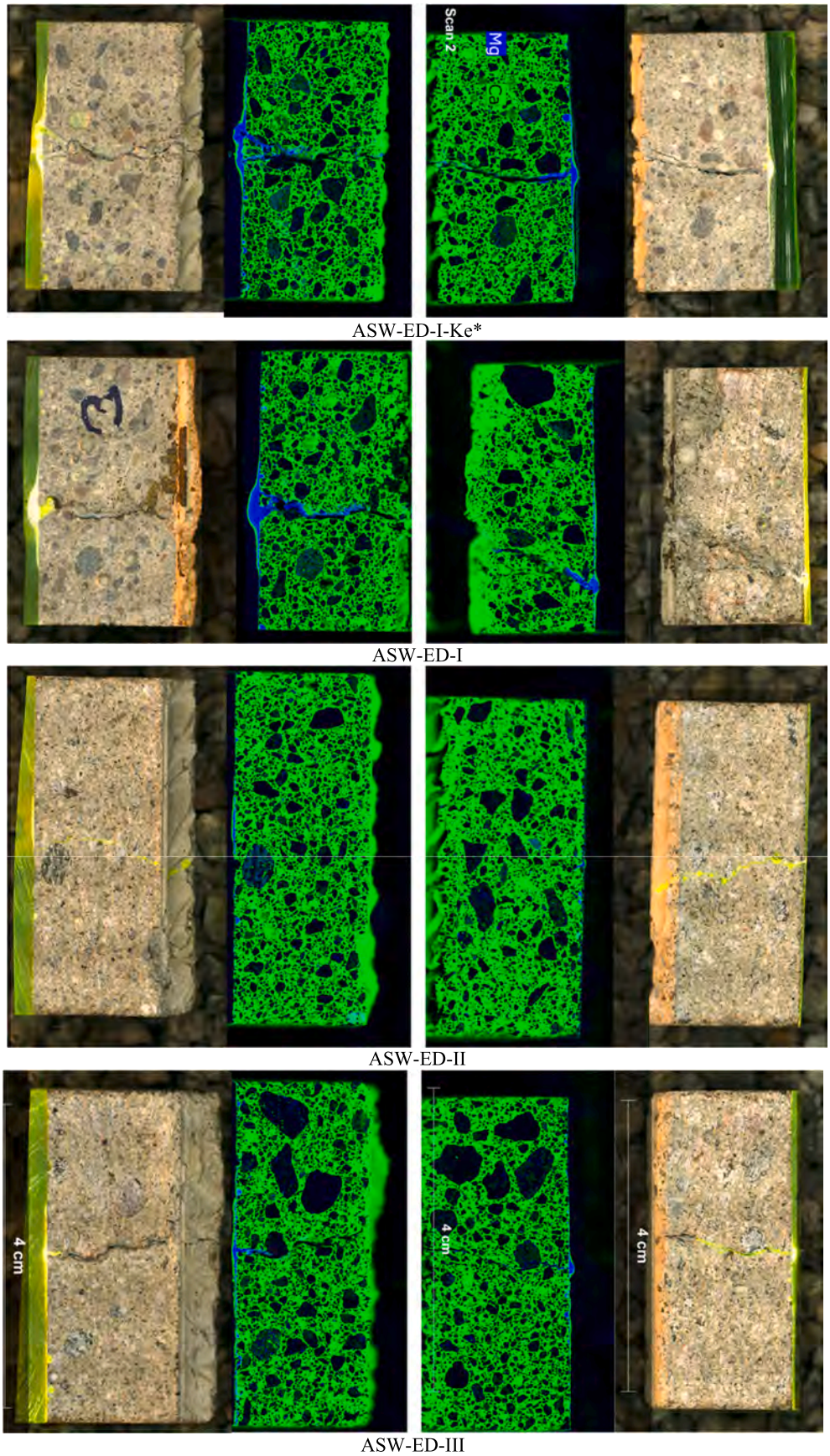

Fig. 7. (*continued*).

cracks, consistent with the observed potential values. In 0-I, only a small amount of brownish coloured material was observed near the largest

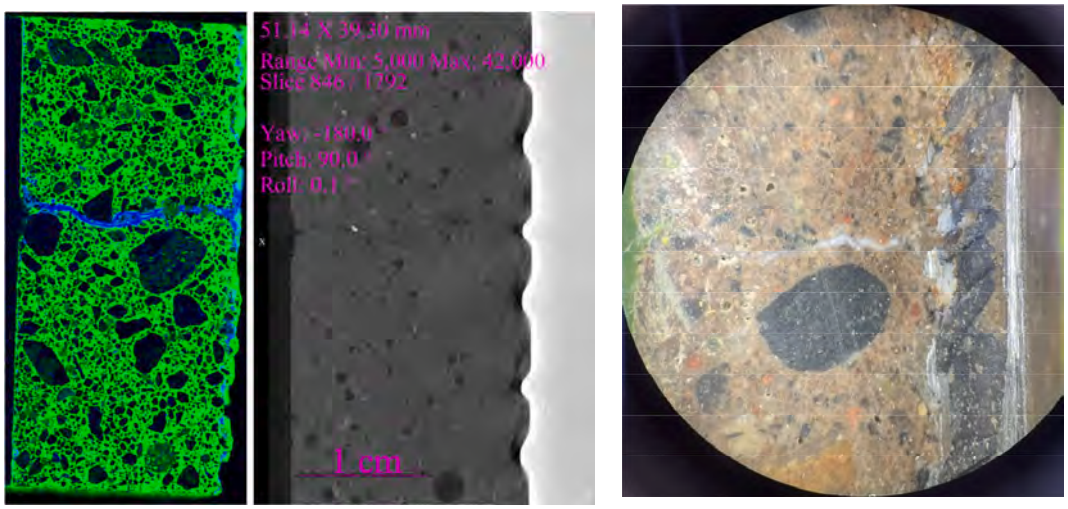

Fig. 8. Crack filling in specimen CMN-ED-I (largest surface crack (0.3-0.75 mm): (a) μXRF mapping of Ca (green) and Mg (blue), (b) CT scan, and (c) optical microscopy. Neon in (c) is the epoxy layer. Left side is the concrete surface in all three images. (For interpretation of the references to colour in this figure legend, the reader is referred to the Web version of this article.)

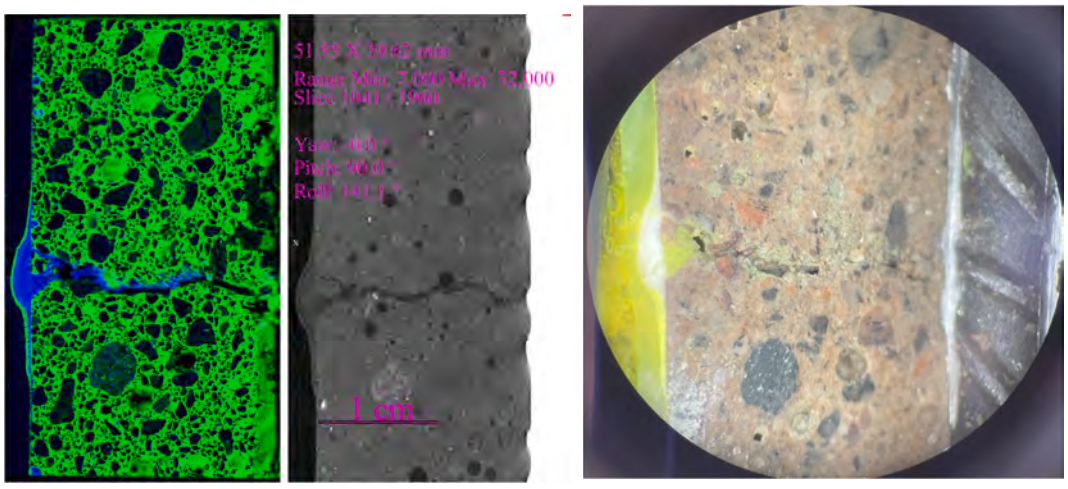

Fig. 9. Crack filling in specimen ASW-ED-I (largest surface crack (0.7-0.75 mm)): (a) μXRF mapping of Ca (green) and Mg (blue), (b) CT scan, and (c) optical microscopy (neon colour on left side is the epoxy layer). Left side is the concrete surface in all three images. (For interpretation of the references to colour in this figure legend, the reader is referred to the Web version of this article.)

Table 6
Summary of results on filling of cracks (where 1,2 represent scan 1 and scan 2 in μXRF and Ke represents kerosene cut specimens) and steel-concrete interface (SCI). NA denotes information not available. Full, Partial, and Empty are qualitative classifications based on image observations within each crack region, each 1/3 of the cover depth.

Specimen	Type of investigation	Surface crack width (mm)	Degree of crack filling, region			Filling of voids at SCI
			Concrete surface-side region	Middle Region	Rebar-side region	
CMN-ED-I	CT	0.3 to 0.75	Full	Full	Difficult to characterise	NA
	μXRF (Mg)[1,2,Ke]		Full to Partial	Full	Full	Yes
	Optical microscopy		Full	Full	Full	Yes
CMN-ED-II	CT	0.1 to 0.3	Full	Full	Difficult to characterise	NA
	μXRF (Mg)[1,2]		Full	Full	Full to Partial	Yes[2]
ASW-ED-I	CT	<0.7 to 0.75	Full	Partial	Difficult to characterise	NA
	μXRF (Mg)[1,2,Ke]		Full to Partial	Partial	Empty	No
	Optical microscopy		Partial	Empty	Empty	NA
ASW-ED-II	CT	≤0.1 to 0.2	Full	Empty	Difficult to characterise	NA
	μXRF (Mg)[1,2]		Partial	Empty	Empty	No
ASW-ED-III	CT	0.25 to 0.45	Full	Partial	Difficult to characterise	NA
	μXRF (Mg)[1,2]		Full to Partial	Partial	Empty	No

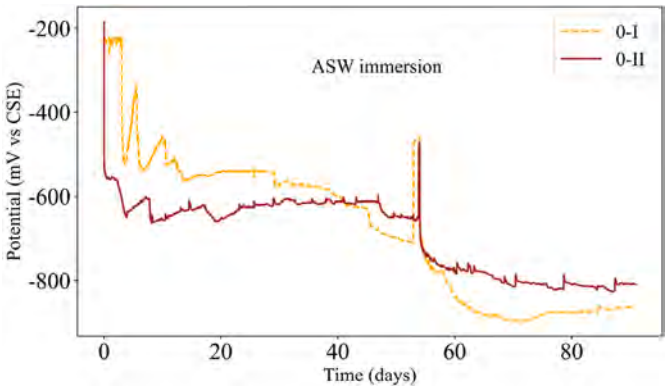

Fig. 10. Half-cell potential of specimens with no treatment (Group 0) during exposure to ASW. Peaks around 55 days are artefacts (see text).

crack (surface crack width 0.15-0.70 mm), see Fig. 16. In 0-II, more pronounced (reddish-brown) corrosion products were clearly visible at the crack mouth of the second largest crack (surface crack width 0.10-0.25 mm), which was located at the very top of the specimen (Fig. 17).

Consistent with the visual observations (Fig. 16c), CT scans revealed corrosion on the reinforcing bar at the largest crack in 0-I, whereas in 0-II, corrosion was observed at the location of the second largest crack of the specimen (Fig. 17c and e). X-ray tomography produces greyscale images in which intensity is linked to material density: denser materials appear brighter, while low-density areas appear darker (almost black). Accordingly, in the CT scans, reinforcing steel bars therefore appear as bright regions corresponding to their high density, while voids are visible as dark regions (low-density areas). Localised corrosion within the rebar is identified by greyish areas, indicating reduced density resulting from the formation of corrosion products. These variations in greyscale intensity provide a clear contrast between intact and corroded steel. Thin, dark (black), thread-like features represent cracks, and round or elliptical black regions indicate macroscopic voids. In specimen 0-I, the CT scans reveal partial migration of corrosion products along the largest crack, indicated by the greyish flow from the corroded rebar region. Fig. 16c further illustrates the deposition of corrosion products in the adjacent void.

The corrosion of the rebars in the vicinity of the crack observed after opening specimens 0-II is illustrated in Fig. 17g–h. This fully aligns with the CT scan results, which reveal corrosion within the respective cracks and correspond to the observed extent of corrosion.

3.6.2. *Corrosion in specimens with treatment*

Visual inspection and CT scan data revealed clear differences in the presence of corrosion among the various treatments. None of the ED-treated specimens in CMN showed signs of corrosion, either visible on the specimen surface or in CT scanning of the rebars. Among the specimens treated with ED in ASW, only one had signs of corrosion in CT scans, which was localised at the widest crack (surface crack width 0.70 to 0.75 mm), while the remaining two specimens showed no corrosion activity (surface crack width 0.1 to 0.3 mm and $\leq$ 0.075 mm). In contrast, both specimens that were initially immersed in the CMN without an applied current and subsequently exposed to ASW exhibited corrosion at their largest cracks in the CT scans (surface crack widths of 0.35 to 0.75 mm and 0.7 to 1.4 mm).

3.6.2.1. CMN immersion (no current). Corrosion is observed in both

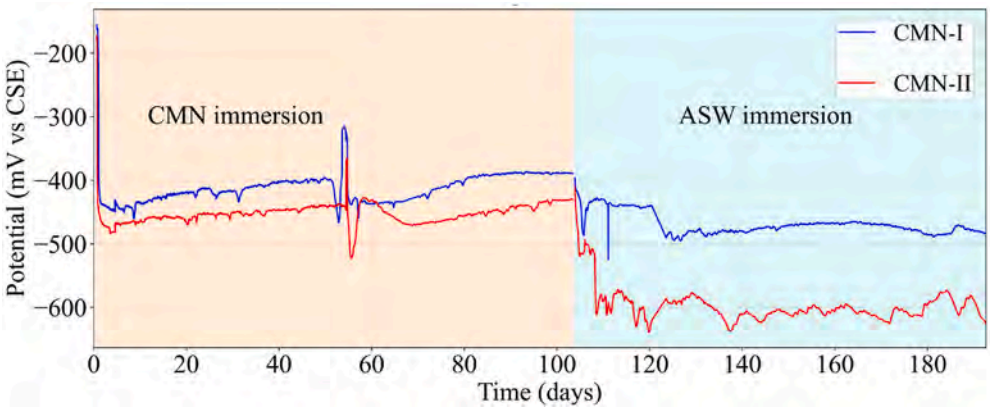

Fig. 11. Half-cell potentials of specimens immersed in Ca-Mg nitrate solution: (left) during treatment in Ca-Mg nitrate solution and (right) during subsequent exposure in artificial seawater (all are open circuit potentials). Peaks around 55 days are artefacts (see text).

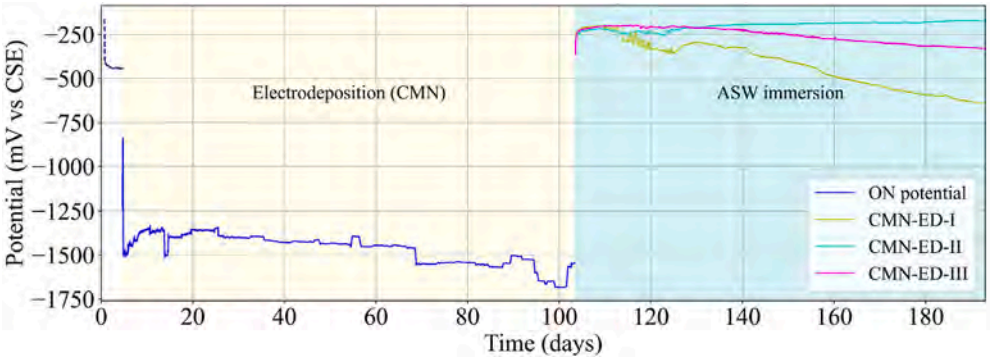

Fig. 12. Half-cell potentials of CMN-ED specimens: (left) during electrodeposition treatment in Ca-Mg nitrate solution (CMN) and (right) during subsequent exposure in artificial seawater (open circuit potentials).

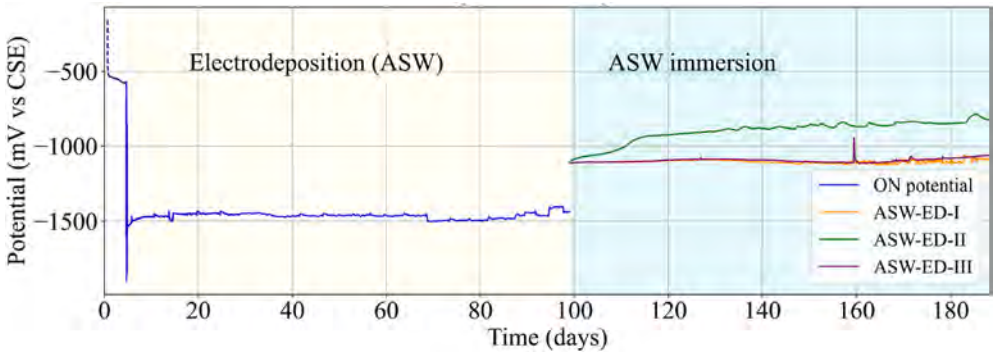

Fig. 13. Half-cell potentials of ASW-ED specimens: (left) during electrodeposition treatment in artificial seawater (ON potentials) and (right) during subsequent exposure in artificial seawater (open circuit potentials).

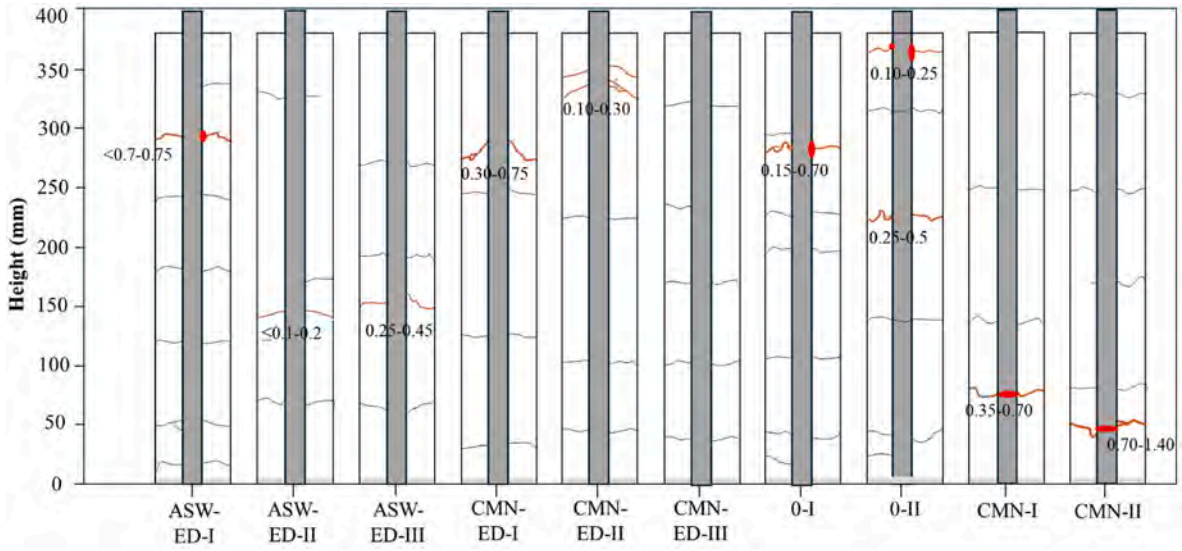

Fig. 14. Schematic representations of location of corrosion (illustrated by red spots in the reinforcement region) observed in CT scans. (Note that CT scans of 0-I and 0-II excluded non-cracked regions). (For interpretation of the references to colour in this figure legend, the reader is referred to the Web version of this article.)

specimens CMN-I and CMN-II in the vicinity of the largest crack, extending around the full circumference of the reinforcement (Figs. 18 and 19). In specimen CMN-II, a bleeding region is detected adjacent to the crack (Fig. 19c).

3.6.2.2. ED treatment with artificial seawater. Fig. 20b illustrates localised corrosion at the largest crack in specimen ASW-ED-I, with corrosion products partially migrating into the crack. Moreover, Fig. 20d shows that large interfacial macroscopic voids are present at the SCI. However, corrosion products were not visible in these regions, probably because these voids were not connected to cracks.

3.6.3. Interfacial macroscopic voids and bleeding zones

Despite the presence of bleeding zones (formed due to segregation, as the specimens lay on one side during the curing period), as illustrated in Fig. 21, no corrosion was detected in these regions, even in the regions where cracks were linked to voids. In CMN-ED-II, this may be related to the effectiveness of ED, as μXRF scans (Fig. 7) showed that almost the entire crack was filled with ED deposits.

3.7. Quantification of reinforcement corrosion

Table 7 summarises the maximum extent of corrosion observed along the length of the rebars. All specimens without ED treatment exhibited corrosion. In specimen 0-I, corrosion extended about 8 mm along the bar and displayed an undercutting, pitting morphology. In specimen 0-II, the largest affected region was smaller (~3.4 mm in length) and remained confined to the surface. Corrosion was also observed in both specimens immersed in CMN. Within ED-treated specimens, no detectable corrosion was observed in the CMN-ED specimens, whereas the ASW-ED-I showed limited corrosion (~2.7 mm in length).

4. Discussion and analytical interpretation

The background of this paper is the potential use of ED for limiting early corrosion initiation at cracks in concrete.

The findings of this study indicate that the effectiveness of ED depends on solution composition, while crack geometry jointly influences deposition patterns and corrosion behaviour. Analytical interpretation was further used to assess the role of solution composition in the underlying electrochemical processes.

Under the parameters of this study, ED in the CMN resulted in deep, relatively uniform internal crack filling, whereas treatment in ASW produced deposits mainly near the crack mouth, with limited penetration toward the SCI. In terms of corrosion behaviour, corrosion was observed in all specimens without ED treatment, while only one of the ED-treated specimens (ASW-ED-I) showed localised corrosion during the exposure period. These observations indicate that electrodeposition can delay corrosion initiation in cracked concrete; however, the results also suggest that the relationship between deposition characteristics and

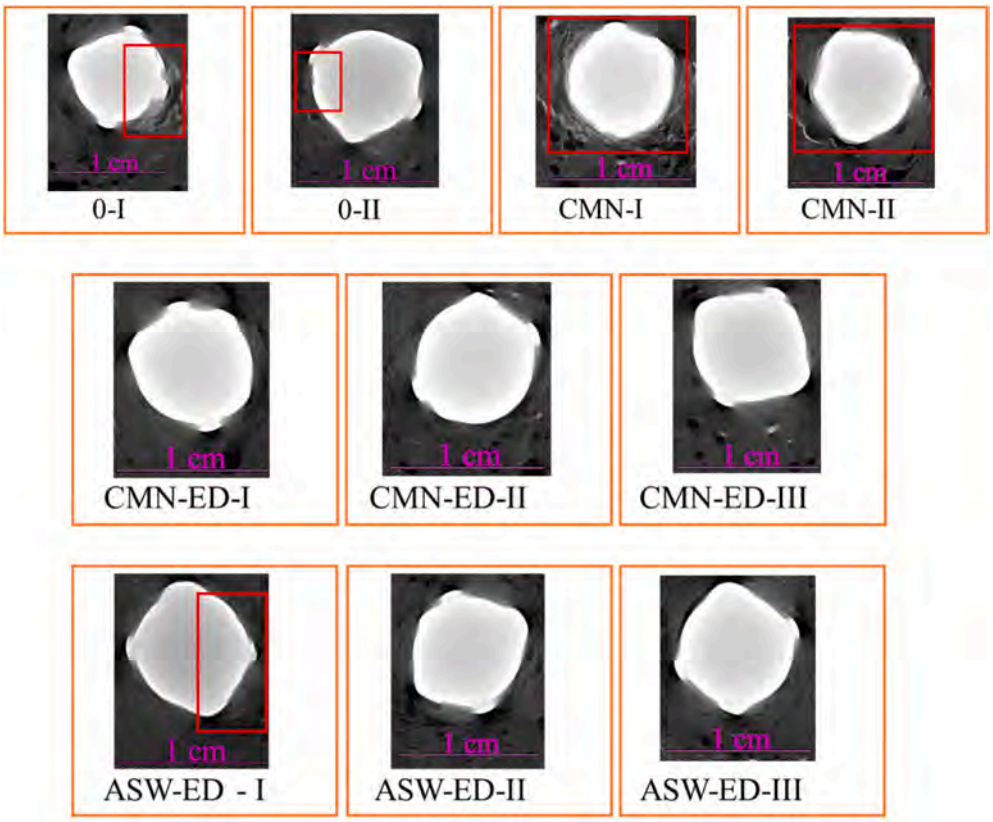

Fig. 15. Reinforcement cross-sections at the largest crack location for all specimens. Red rectangles indicate regions where corrosion was observed. (For interpretation of the references to colour in this figure legend, the reader is referred to the Web version of this article.)

corrosion performance is not straightforward. The findings therefore highlight the importance of electrolyte composition for deposition behaviour, while indicating that additional factors may influence the resulting corrosion performance.

This interpretation is supported by the combined use of visual inspection, CT scanning, μ-XRF elemental mapping, and optical microscopy, which provided information on crack morphology, crack filling, and corrosion. Visual inspection indicated deposits on the surfaces of the ED-treated specimens (CMN-ED and ASW-ED), while corrosion products were mainly observed on the untreated specimens (0 and CMN), except for specimen ASW-ED-I (Figs. 15–20). μXRF elemental mapping revealed nearly complete internal crack filling in the CMN-ED specimens, whereas the ASW-ED specimens showed deposition primarily near the crack mouth with limited penetration toward the SCI (Figs. 7–9). Optical microscopy of selected specimens confirmed these filling patterns and supported the interpretation of the CT scans.

4.1. Influence of electrolyte composition on ED deposits

According to previous studies, electrolyte composition and Mg^{2+} concentration play a critical role in ED efficiency, with nitrate-based electrolytes showing strong ED performance. As summarised by Chen et al. [17], tests reported by Otsuki et al. (2002) [21] demonstrated that a 0.1 mol/L $Mg(NO_3)_2$ electrolyte at a current density of 1.0 A/m^2 achieved crack coverage ratios of approximately 72% after 7 days and 98% after 56 days, highlighting the strong performance of Mg nitrate-based solutions for crack filling. At higher $Mg(NO_3)_2$ concentration of 0.25 mol/L, Chu et al. (2012) [20] reported approximately 95% crack closure within 20 days at 2 A/m^2. However, the corresponding crack-filling depth was relatively shallow (~6.5 mm). Crack geometry and the performance metric must therefore be considered alongside electrolyte composition when comparing electrodeposition performance across studies.

Fig. 22 highlights a clear and systematic influence of electrolyte composition on the penetration depth of Mg electrodeposits. Specimens treated with the CMN exhibited consistently high filling degrees, with crack filling depths approaching the full crack depth (≈18 mm) across all investigated crack widths. This behaviour is consistent with the higher availability of magnesium (and calcium) ions in the CMN, which contained 0.5 M $Mg(NO_3)_2$. In contrast, specimens treated with ASW showed markedly lower filling depths, which is in line with the substantially lower Mg^{2+} availability in ASW (≈0.05 mol/ L). Overall, Fig. 22 indicates that an increased magnesium ion concentration in the electrolyte is associated with improved crack-filling, highlighting the importance of electrolyte composition for achieving deep and consistent filling.

4.1.1. Analytical interpretation of mass transport and precipitation during ED treatment

To understand the observed crack-filling and deposition patterns, a simplified analytical model of mass transport and reactions occurring during ED treatment in both CMN and ASW was established (see Fig. 23). This interpretation should be seen as a semi-quantitative first attempt. It should be noted that the mineral phases are not identified experimentally in this study; $Mg(OH)_2$ and $Ca(OH)_2$ are considered only as possible products in the analytical interpretation. Amounts of deposits are estimated as follows. From the charge passed in the CMN experiment (see Table 2), 2.19 mol of electrons were released in the system (three specimens), producing hydroxyl ions (base) at the steel surface through the cathodic reaction $2H_2O + 2e \rightarrow H_2\,(g) + 2\,OH^-$ and suggesting the potential formation of about 1.1 mol $Mg(OH)_2$ (≈27 cm^3 solid material across three specimens). This theoretical amount is of similar magnitude to the total crack volume (for three cracks of 0.5 mm width), indicating that the applied ED treatment could completely fill

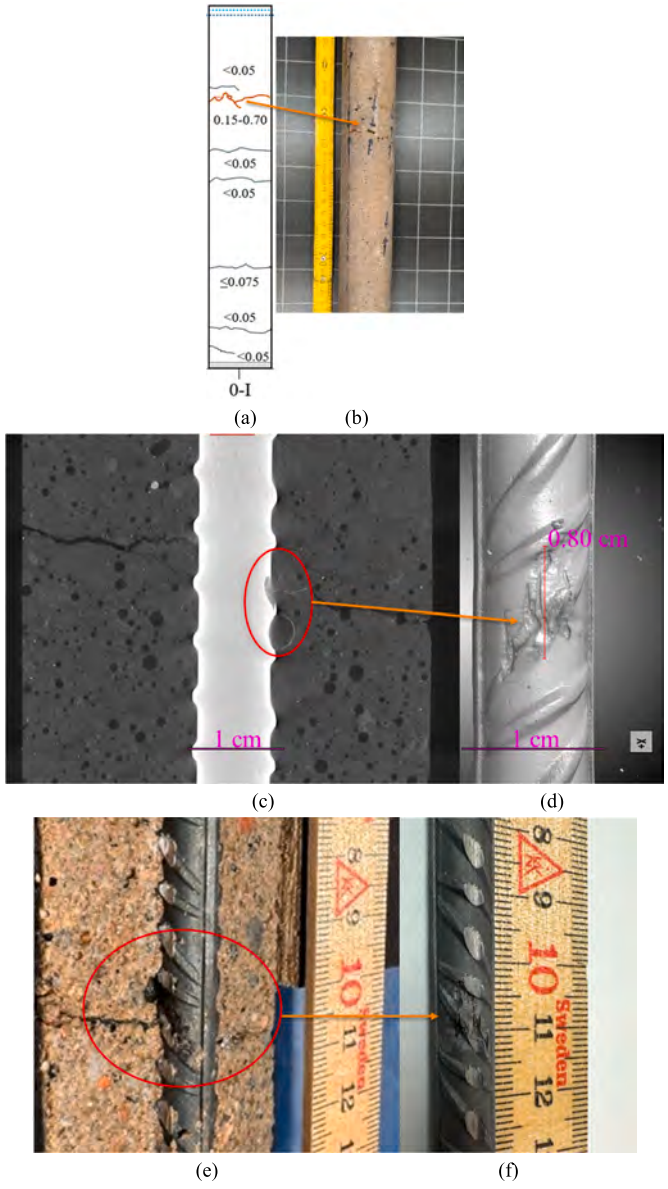

Fig. 16. Summary of observations at the major crack in Specimen 0-I (surface crack width 0.15-0.70 mm): (a) Crack location, (b) Visual appearance of corrosion on the concrete surface of specimen, (c) CT scan sections showcasing corroded region in vicinity of the crack, (d) 3D volume of reinforcement bar, segmented from CT data (threshold range: 35000 to 49000) showcasing corroded region of the bar, (e) Corroded region after destructive testing, and (f) Corroded region at the reinforcement after cleaning the rebar.

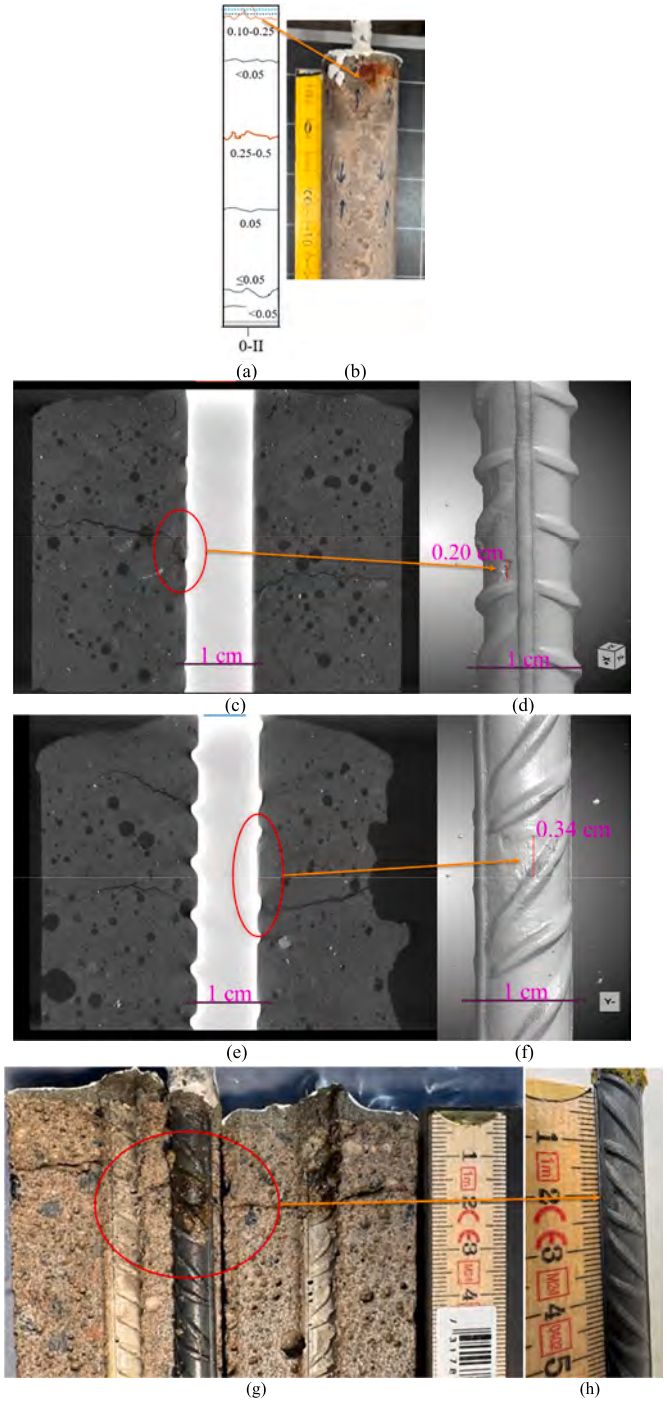

Fig. 17. Summary of observations at the second largest crack in Specimen 0-II (surface crack width 0.10 to 0.25 mm): (a) Crack location on specimen 0-II, (b) Visual appearance of corrosion on the surface of specimen, (c) CT scan showcasing corroded region in vicinity of the second largest crack, (d) corresponding 3D visualisation of the rebar obtained from CT scans, showing the corroded region, (e) and (f) CT scan and corresponding 3D visualisation of the reinforcement on the opposite side of the second largest crack, (g) Visual inspection of location of corrosion after destructive testing, and (h) Corroded region on the reinforcement after cleaning the rebar. For all 3D visualisations, the rebar was segmented using a threshold of 37000-49000.

one crack about 0.5 mm wide in each specimen, as observed in several of the investigated specimens. The corresponding anodic reaction $H_2O \rightarrow ½ O_2 (g) + 2 H^+ + 2e$ produces an equivalent amount of acid, accounting for the experimentally observed decrease in solution pH to approximately 3 after treatment (see Fig. 6). The specimens themselves act as physical separators, preventing direct mixing of acid and base products and thereby sustaining strong pH gradients across the system.

The solution composition and measured conductivity variations provide further insight into ion transport. Initially, both CMN (0.5 M Ca^{2+} + 0.5 M Mg^{2+}) and ASW solutions were near neutral, but upon application of current, both became acidic. The conductivity in CMN decreased by nearly 20% (see Fig. 6). This drop indicates a significant removal of Ca^{2+} and Mg^{2+} ions from the solution, consistent with precipitation of hydroxides.

The high resistance of the uncracked parts of the specimens, based on an estimated concrete resistivity of 120 Ω m (based on voltage and current data), and the low CMN resistivity (≈0.1 Ω m) suggest that wide cracks act as preferential current pathways, resulting in local current densities up to several hundred A/m^2, far exceeding the nominal 1 A/

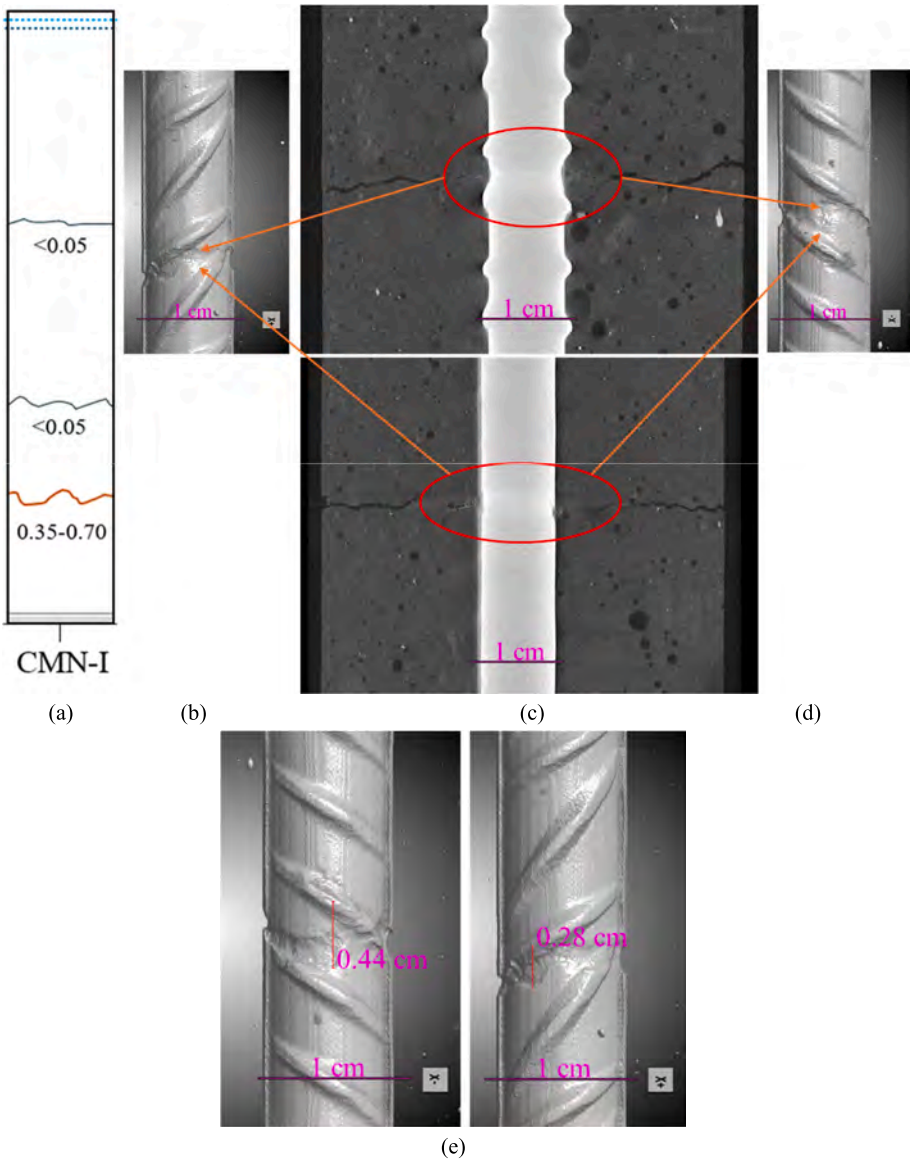

Fig. 18. (a) Crack location on specimen CMN-I, (b) and (d) 3D visualisation of corroded region at the rebar in respective regions obtained from CT scans, (c) CT scans of the specimen showing corroded region at the vicinity of the largest crack along with partial flow of corrosion products in the crack, and (e) corresponding 3D visualisation of the rebar obtained from CT scans, showcasing the maximum length of corroded region around the circumference of the rebar. For all 3D visualisations, the rebar was segmented using a threshold of 34000-42000.

m^2. Consequently, current distribution is highly uneven: most current flows through wider cracks, generating locally higher OH^- concentrations, which promote intense precipitation. This is supported by a measured increase in resistance over time (from ~10 Ω to 24 Ω over 98 days of ED, for three specimens in parallel). Based on resistance estimates from voltage and current data, solution conductivity, and crack geometry, Table 8 provides estimated currents through the bulk concrete and the cracks in the three specimens in CMN with different crack widths. A 6 mA current through the crack in CMN-ED-I sustained for 98 days could theoretically deposit 15 g (≈6 mL) of $Mg(OH)_2$, enough to nearly fill a 0.5 mm wide crack, in agreement with experimental evidence of an almost completely filled crack.

The specimens treated by electrodeposition show contrasting behaviour in CMN and ASW solutions. In CMN, high cation concentrations ensure immediate reaction between locally produced OH^- and Mg^{2+}/Ca^{2+}, leading to precipitation directly at the steel surface and progressive inward-to-outward crack filling. In ASW, where the Mg^{2+} concentration is an order of magnitude lower, the OH^- generated at the cathode migrates outward before encountering sufficient Mg^{2+}, resulting in $Mg(OH)_2$ deposition predominantly near the crack mouth. Thus, CMN promotes internal filling and structural densification, whereas ASW tends to form surface near fillings. The proposed interpretation, as illustrated in Fig. 23, should be seen as a starting point for further refinement.

This prediction aligns well with the experimental findings (Section 3.4) discussed in Section 4.3, where image-based analyses confirm internal crack filling in CMN-ED specimens and surface-limited deposition in ASW-ED specimens.

4.2. *Influence of crack geometry*

Based on the results in Table 6 and the discussion in Section 4.1, it appears that electrolyte composition governs the overall extent of electrodeposition, whereas the influence of crack geometry is less pronounced and cannot be isolated conclusively. All except one specimen exhibited a single dominant crack after unloading; specimen CMN-ED-II

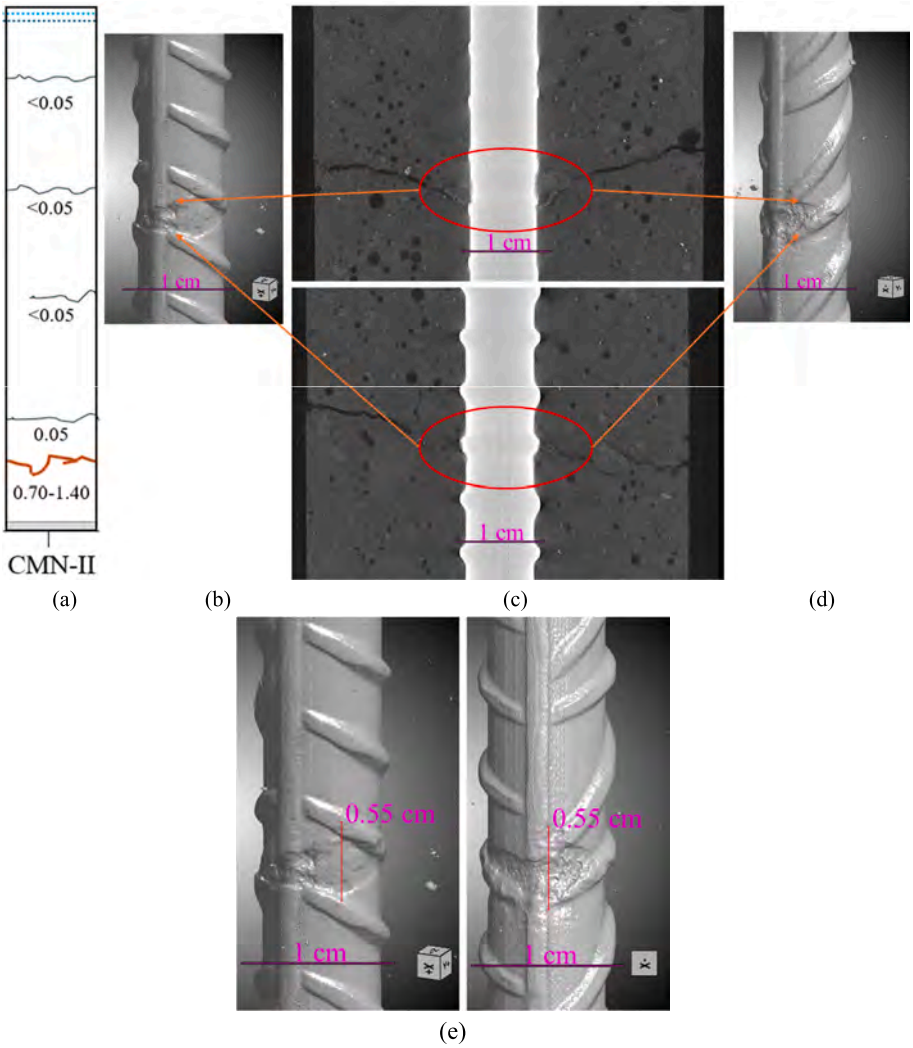

Fig. 19. (a) Crack location on specimen CMN-II, (b) and (d) 3D visualisation of corroded region at the rebar in respective regions obtained from CT scans, (c) CT scans of the specimen showing corroded region at the vicinity of the largest crack along with partial flow of corrosion products in the crack, and (e) corresponding 3D visualisation of the rebar obtained from CT scans, showing the maximum circumferential extent of the corroded region. For all 3D visualisations, the rebar was segmented using a threshold of 34000-42000.

had two dominant cracks. In the present study, comparisons were based on the largest visible crack in each specimen, whereas multiple cracks were not treated as an independent variable.

The CMN-ED specimens exhibited deposition over a greater portion of the crack depth. In CMN-ED specimens, differences in the apparent filling distribution were observed between narrower and wider cracks, but no systematic trend could be established with confidence based on the available data. The observations suggest that electrolyte composition played the primary role in filling the cracks, whereas no clear systematic dependence on crack width was evident within the investigated dataset.

In contrast, for ASW-ED specimens, deposition was largely restricted to the near-surface part of the crack across all investigated surface crack widths (wider than 0.1 mm), with limited filling in the middle and near-bar regions. Moreover, from Fig. 22, it can be seen that, in ASW-ED specimens, wider cracks were associated with higher penetration depths in some cases, whereas narrower cracks showed shallower filling, as observed for ASW-ED-II and ASW-ED-III. A similar tendency has been reported in some earlier ED studies. Ryu [27] reported that deposition depth increased from about 2 mm to 8 mm as crack width increased from 0.2 to 1.0 mm in 0.1 mol/L $ZnSO_4$, while Ryou [28] observed a greater deposition depth for 0.5 mm cracks than for 0.1 mm cracks in 0.1 mol/L $MgCl_2$. These observations suggest that, for ASW-ED specimens, crack width may influence deposition behaviour. However, the limited number of specimens in the present study, together with differences in electrolyte composition and test conditions across studies, precludes a definitive assessment of the underlying mechanisms.

4.3. *Effect of ED treatment on corrosion behaviour*

The combined results from half-cell potential measurements (Section 3.4), observation based on CT scan data (of all specimens), and visual inspection of rebars after opening the specimens (for two specimens) demonstrate that ED significantly influenced corrosion behaviour during the 3-month ASW exposure. Direct experimental evidence linking electrodeposition-induced crack filling to corrosion performance under such exposure conditions remains limited in the literature, and the present results therefore provide new insight into this relationship.

4.3.1. *Half-cell potential*

Half-cell potential measurements indicate that specimens in the 0 and CMN groups (i.e., non-ED-treated specimens) exhibited corrosion during three months of ASW immersion, consistent with other characterisation results. Values ranged from - 500 to −800 mV_{CSE}. The

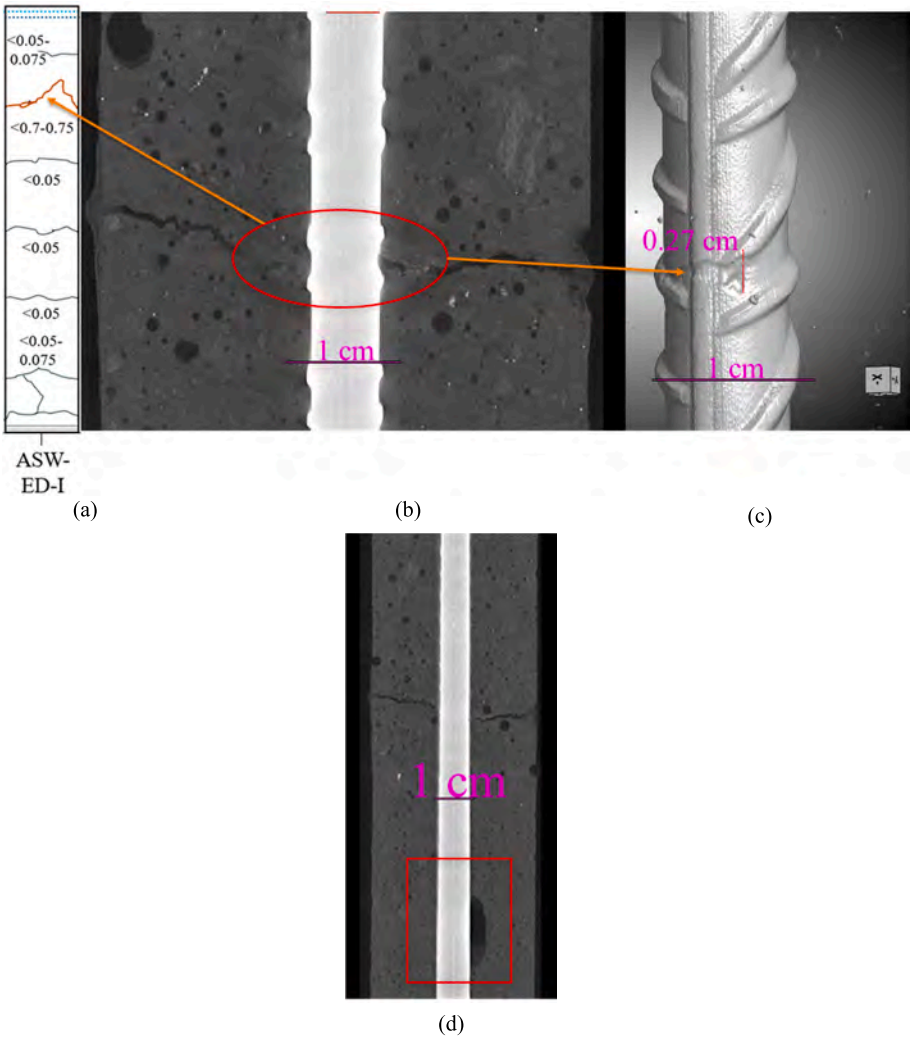

Fig. 20. (a) Crack location on the specimen ASW-ED-I, (b) CT scan of the specimen showing corroded region at the vicinity of the largest crack along with the flow of corrosion products in the crack, (c) corresponding 3D visualisation of the rebar obtained from CT scans, showing the corroded region (rebar segmentation threshold: 30000-42000), and (d) Presence of macroscopic voids in the steel–concrete interface.

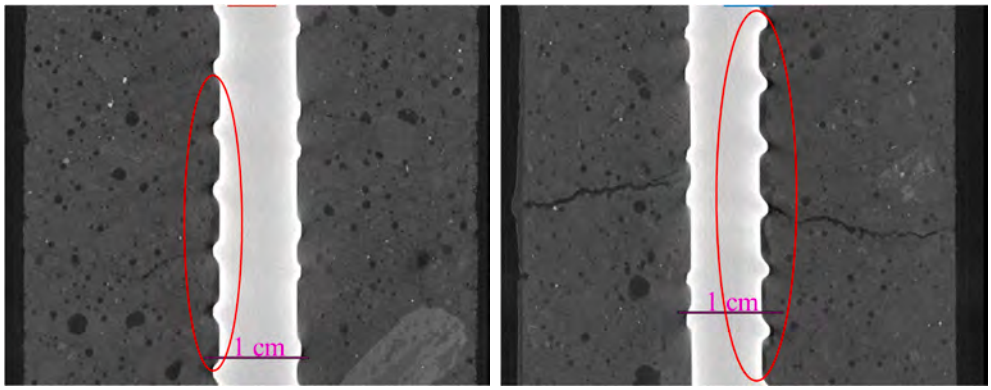

Fig. 21. CT scans of specimens CMN-ED-II (left) and ASW-ED-III (right) showing macroscopic voids at the steel-concrete interface.

observed trends agree with [29], who reported corrosion initiation at potentials in the range −550 to −600 mV_{CSE}, under submerged conditions, −400 to −550 mV_{CSE} being the intermediate range.

In contrast, the ASW-ED specimens maintained potential below −1000 mV_{CSE} after treatment, suggesting delayed depolarisation after current switch-off. Specimens ASW-ED-I and ASW-ED-III remained stable (−1070 to −1120 mV_{CSE}), whereas ASW-ED-II showed a gradual increase to −850 mV_{CSE}, indicating progressive depolarisation. Delayed depolarisation behaviour in reinforced concrete specimens has been reported by Ref. [7] after realkalisation, i.e., high-current-density treatment, highlighting the time-dependent nature of potential recovery under submerged conditions. In the present study, however, delayed

Table 7
Maximum corrosion length observed in CT scans.

Specimen	Surface crack width (mm)	Maximum corroded length along the vertical axis of rebar (mm)	Macroscopic voids at SCI interconnected with crack	Remarks
0-I	0.15 to 0.70	8.0	No	Corrosion was observed only on one side of the rebar at the crack
0-II	0.10 to 0.25	3.4	No	Corrosion was observed on both sides of the rebar at the crack
CMN-I	0.35 to 0.70	4.4	No	Corrosion was observed around the entire circumference
CMN-II	0.70 to 1.40	5.5	Yes	Corrosion was observed around the entire circumference
CMN-ED-I	0.3 to 0.75	-	Yes	Corrosion not observed
CMN-ED-II	0.1 to 0.3	-	Yes	Corrosion not observed
CMN-ED-III	all < 0.1 mm	-	No	Corrosion not observed
ASW-ED-I	<0.7 to 0.75	2.7 mm	No	Corrosion was observed only on one side of the rebar at the crack
ASW-ED-II	≤0.1 to 0.2	-	Yes	Corrosion not observed
ASW-ED-III	0.25 to 0.45	-	Yes	Corrosion not observed

depolarisation persisted over several months. Although further depolarisation and corrosion may occur over longer exposure periods, the ASW-ED specimens remained protected throughout the experiment, except for one specimen.

4.3.2. *Effect of cracks on corrosion resistance*

Specimens without ED treatment showed corrosion localised at the largest cracks, consistent with half-cell potential monitoring and CT scans (Figs. 9–19). It should be noted that in specimens in the 0 group, the corrosion was localised, whereas in the CMN specimens, corrosion extended around the entire rebar circumference at the location of the widest crack. However, it should be noted that corrosion was never observed simultaneously at different cracks within the same specimen. The results demonstrated that wider cracks directly influence the initiation and propagation of corrosion, and that partial or incomplete filling (as in ASW-ED specimens) may also leave the steel vulnerable.

Interfacial macroscopic voids connected to cracks may influence both ion transport and corrosion initiation by providing additional pathways along the steel-concrete interface. As shown in Table 5, this connectivity varies between specimens. Despite the presence of bleeding zones and interfacial macroscopic voids along the SCI in both CMN-ED and ASW-ED specimens (see Table 7), no corrosion was observed in these regions. In contrast, corrosion was observed at the cracks in the untreated reference specimens 0-I and 0-II, which had interfacial macroscopic voids, but not connected to the largest cracks. In the CMN group, CMN-II had a connected interfacial macroscopic void, whereas CMN-I did not. Among the ED-treated specimens, connected interfacial macroscopic voids were observed in CMN-ED-I, CMN-ED-II, ASW-ED-II, and ASW-ED-III, whereas CMN-ED-III and ASW-ED-I did not show such connectivity. No corrosion was observed in CMN-ED-I and CMN-ED-II despite the presence of connected interfacial macroscopic voids. Thus, interfacial macroscopic void connectivity should be considered when interpreting specimen-to-specimen differences in crack filling and corrosion response; however, the observed corrosion behaviour cannot be attributed to void connectivity alone.

This suggests that under the applied experimental conditions, ED effectively protected the steel even in the presence of voids, and that voids—either isolated or connected to cracks—did not necessarily exacerbate corrosion when cracks were adequately filled, or no pathway was present for ingress of chlorides.

4.3.3. *Overall effectiveness of electrodeposition in limiting corrosion*

Overall, the ED applied was effective in mitigating corrosion at cracks during the three-month exposure to ASW, particularly for specimens treated in CMN, where almost full crack filling was achieved. In these specimens, no corrosion was observed, consistent with expected reduced chloride access to the steel surface due to crack filling by the electrodeposited products. In contrast, the ASW-based treatment

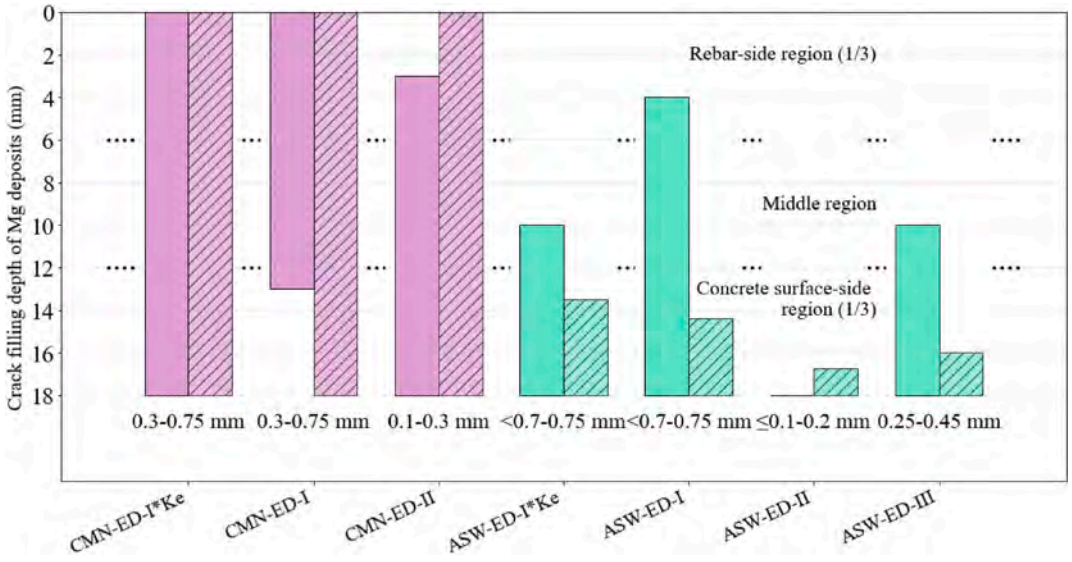

Fig. 22. Depth of crack filling measured on μ-XRF Mg-maps of two adjacent surfaces of the same section. The numbers are the measured surface crack widths. 'Ke' denotes specimens sectioned using kerosene cooling when cutting. Note that the maximum crack depth is 18 mm, the cover to the steel bar. 18 mm denotes the concrete surface, and 0 denotes the steel–concrete interface.

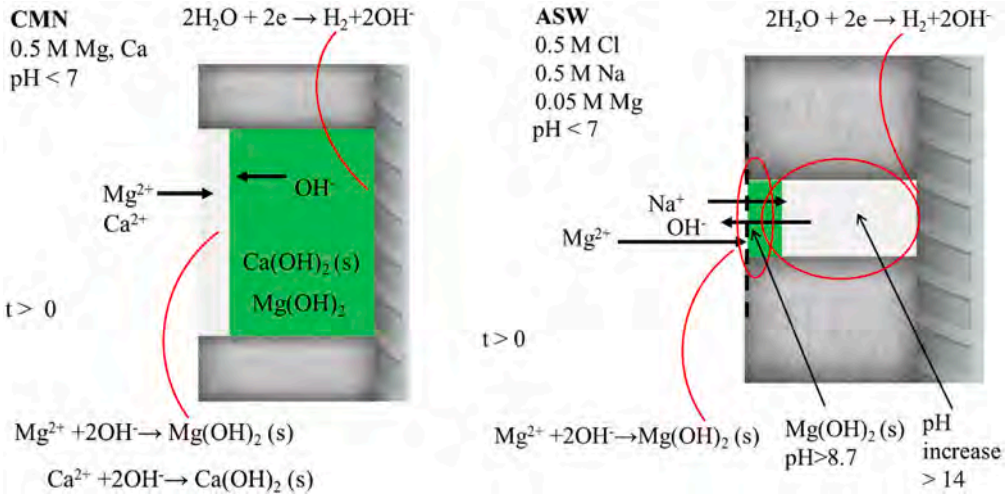

Fig. 23. Simplified analytical model of mass transport and reactions occurring during electrodeposition treatment in Ca-Mg nitrate solution (left) and artificial seawater (right), illustrating progressive precipitation of solids in the crack. The high concentration of Mg and Ca in the Ca-Mg nitrate solution causes precipitation near the steel (left), while the limited Mg in artificial seawater is precipitated already near the crack tip (right).

Table 8
Estimated currents through specimens and cracks.

Specimen	Assumed crack width (mm)	Current (mA)		
		Concrete	Crack	Specimen
CMN-ED-I	0.5	6	6	12
CMN-ED-II	0.2	6	2	8
CMN-ED-III	0	6	0	6

resulted in partial filling, and corrosion was delayed but not fully prevented; corrosion was observed in one specimen, while it was not detected in the two others despite incomplete filling. While electrodeposited material may block or slow down chloride ingress, the direct effect of ED on chloride transport cannot be conclusively assessed in the present study due to masking by the chloride-containing epoxy resin, as illustrated by the elemental maps in Fig. 24 (chloride shown in red). It should be noted that given the limited number of specimens in each group, the present findings should be interpreted in terms of comparative trends under the controlled laboratory conditions used in this study, rather than as a basis for generalisation.

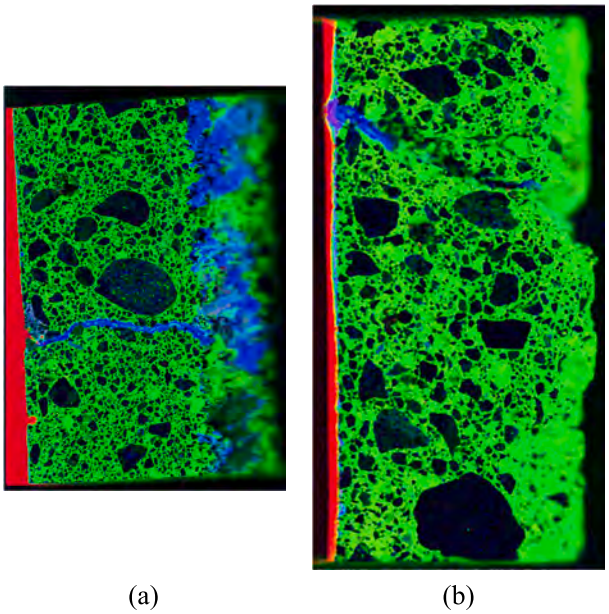

Fig. 24. Elemental map showing Ca (green), Mg (blue), and Cl (red); the chlorine signal originates primarily from the chloride-containing epoxy at the specimen surface: (a) CMN-ED-I specimen (Scan 2) and (b) ASW-ED-I specimen (Scan 2). Please note, massive Mg deposits at the steel–concrete interface. (For interpretation of the references to colour in this figure legend, the reader is referred to the Web version of this article.)

5. Conclusions

Ten reinforced concrete specimens cracked in tension with and without the application of cathodic current were investigated. The application of cathodic current was intended to induce electrodeposition (ED) within the cracks, either from a calcium-magnesium nitrate solution (CMN) or from artificial seawater (ASW). The extent and location of the deposits, as well as the extent of the corrosion attack at the cracks, were studied after a period of exposure to ASW. Multiple techniques were used to monitor and assess corrosion non-destructively and to characterise the deposits, while destructive assessment of rebar corrosion was performed on two specimens. In addition, a simplified analytical interpretation of mass transport and deposition was used to help understand the various processes.

1) The filling of cracks was found to differ between the electrolytes CMN and ASW, despite equal amounts of charge being applied.
   - CMN-ED outperformed ASW-ED. CMN-ED produced uniform internal filling due to high concentration of Mg^{2+} and Ca^{2+}, and no corrosion was observed during the three-month post-treatment exposure in ASW. In contrast, ASW-ED resulted in crack filling near the surface but incomplete internal filling due to a lower concentration of Mg^{2+}/Ca^{2+}; one specimen with the widest crack (<0.7 to 0.75 mm) showed localised corrosion at that crack after subsequent exposure.
   - Analytical interpretation of ED in CMN showed that cracks were filled progressively inward-to-outward due to the high concentration of Mg^{2+} and Ca^{2+}, whereas, in ASW, the lower concentration of Mg^{2+} led to deposition starting mainly at the crack mouth/concrete surface.
2) The influence of surface crack width and crack geometry on ED deposits was found to be solution dependent.
   - CMN-ED: Cracks wider than 0.1 mm were filled internally; the combined μXRF, optical microscopy, and analytical model

indicated ED deposits inside the cracks. Even for the widest cracks (0.3 to 0.75 mm), interior deposits were observed throughout the crack depth but did not completely fill the crack, and hence no dependence on crack width was observed.
- ASW-ED: The specimen with wider cracks (<0.7 to 0.75 mm) tended to show deposits at deeper depth, indicating a possible influence of crack width on filling behaviour, although the available data were insufficient to establish a definitive relationship.

3) Deposition was also observed to occur in some of the macroscopic voids (possibly formed due to segregation) at the steel–concrete interface.
   - From the μXRF results, it was clearly observed that interfacial macroscopic voids along the rebar at both sides of the crack were filled with Mg deposits in the CMN-ED-I specimen, as far as they were connected to the cracks.
4) Without ED treatment, notable corrosion was observed at the rebars at the crack locations in the experimental setup used.
   - Cracks strongly governed corrosion initiation and localisation. In specimens exposed only to ASW and in specimens first immersed in CMN (without current) and subsequently in ASW, corrosion was consistently localised where the largest surface cracks crossed the rebars. Corrosion was indicated by half-cell potential measurements and confirmed by CT scanning, which showed corrosion and formation of corrosion products along cracks.
5) During the three-month seawater exposure following ED treatment, corrosion of the embedded reinforcing bars at crack locations was influenced by the ED treatment, with its effectiveness depending on the electrolyte composition and the crack geometry.
   - Corrosion was prevented in all three specimens (maximum surface crack width 0.75 mm) that underwent ED treatment in CMN, probably due to deep and continuous internal filling of the cracks and the interconnected macroscopic voids at the steel-concrete interface.
   - Corrosion was prevented in two of three specimens ED treated in ASW. The one corroded was much less compared to specimens not treated with ED. This suggests that the ED treatment contributed to corrosion prevention during the three-month corrosive exposure period despite limited/partial crack filling.

Appendix

Specimen end protection.

CRediT authorship contribution statement

Suraksha Sharma: Conceptualization, Data curation, Investigation, Methodology, Writing – original draft. **Karla Hornbostel:** Conceptualization, Methodology, Validation, Writing – review & editing. **Rob Polder:** Conceptualization, Formal analysis, Writing – review & editing. **Samanta Robuschi:** Conceptualization, Methodology, Writing – review & editing. **Karin Lundgren:** Conceptualization, Writing – review & editing. **Tobias Danner:** Formal analysis, Writing – review & editing. **Roy Johnsen:** Methodology, Writing – review & editing. **Mette Rica Geiker:** Conceptualization, Supervision, Writing – review & editing.

Declaration of generative AI and AI-assisted technologies in the manuscript preparation process

During the preparation of this work, the authors used OpenAI's ChatGPT to assist with drafting Python code for preparing graphs. After using this tool, the authors reviewed and edited the content as needed and take full responsibility for the content of the publication.

Declaration of competing interests

The authors declare that they have no known competing financial interests or personal relationships that could have appeared to influence the work reported in this paper.

Acknowledgements

The authors gratefully acknowledge the financial support provided by the Swedish Transport Administration through the CraCor2 project (Cracks and Reinforcement Corrosion, Project ID: 2023/32344) and the Research Council of Norway through THE EXCON project (Green Management of Structures for Infrastructure, Project No. 340843). The authors would like to gratefully acknowledge Protector AS, Norway, for its assistance with the CAMUR setup; Peter Laugesen, Pelcon Materials & Testing ApS, Denmark, for support with epoxy impregnation; Stephen Hall, 4D Imaging Lab, Lund University, for assistance with CT scanning; Camilla Lindström, RISE Research Institutes of Sweden, for performing μXRF elemental mapping; and Lovise Sjöqvist, RISE Research Institutes of Sweden, for facilitating the coordination of the μXRF work.

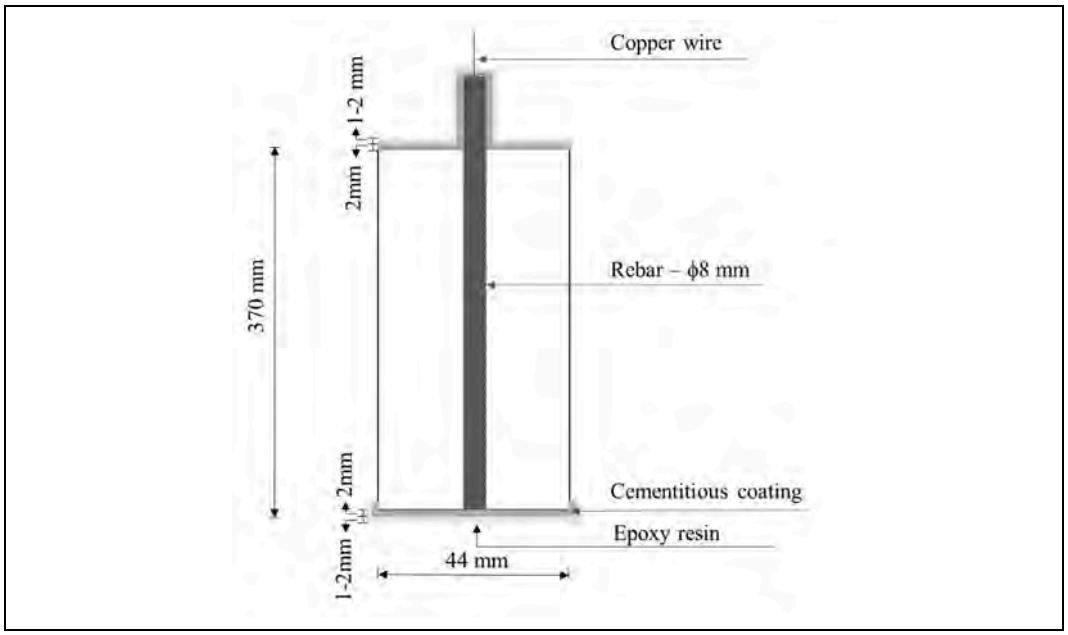

Fig. A1. Schematic illustration of the specimen end protection, showing the cementitious coating, epoxy coating, and protected protruding reinforcement.

Elemental maps from μXRF analysis.

CMN-ED-I Ke*	CMN-ED-I	CMN-ED-II	
ASW-ED-I Ke*	ASW-ED-I	ASW-ED-II	ASW-ED-III
Ke*: Specimens cut using Kerosene			

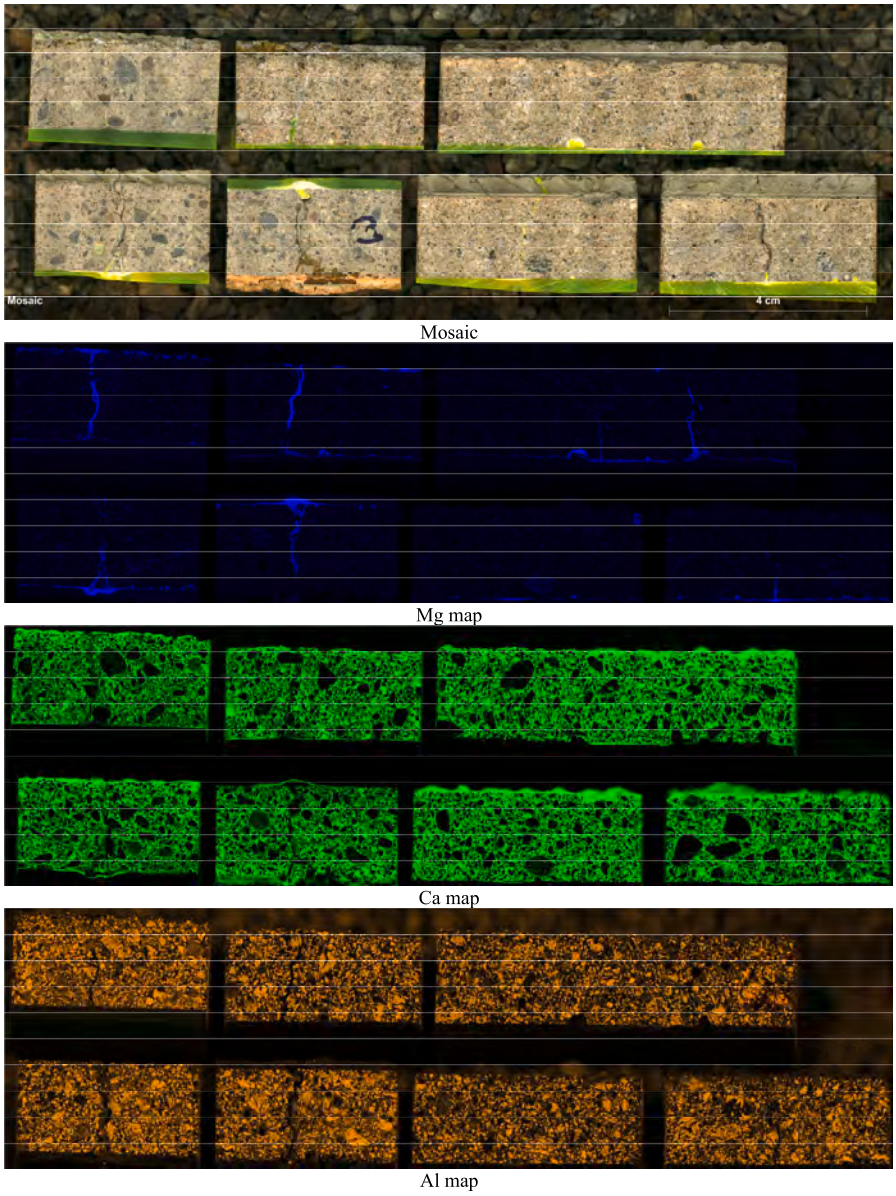

Fig. A2. Elemental mapping of electrodeposited specimens (Scan 1).

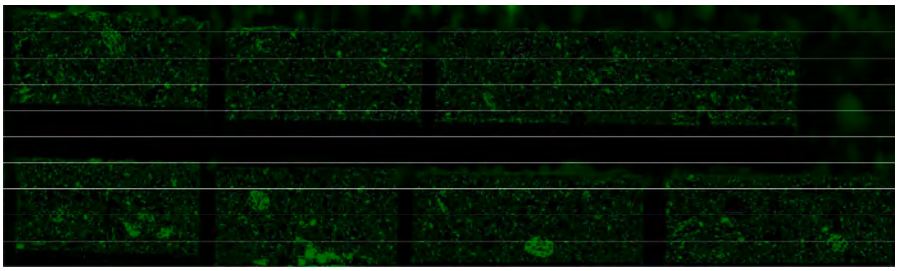

Fe map

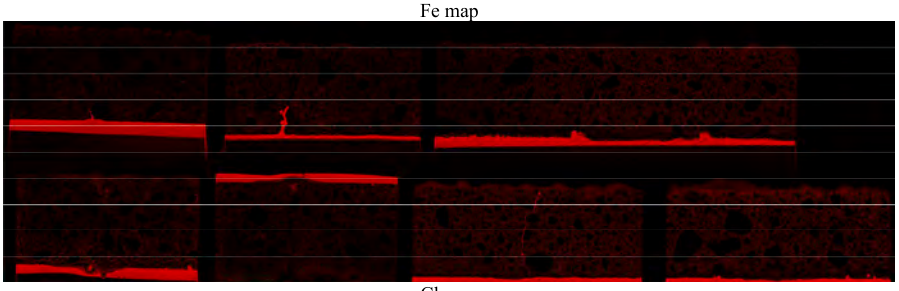

Cl map

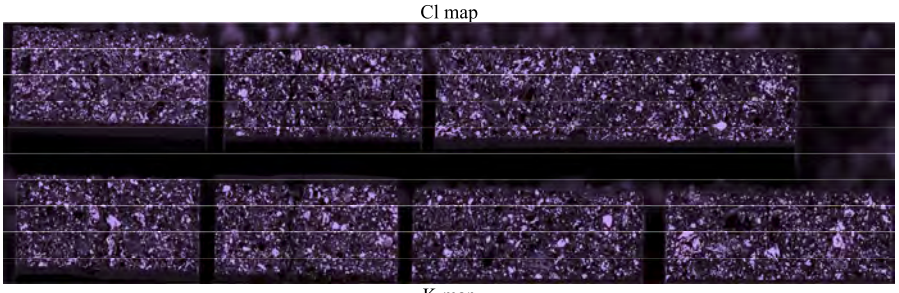

K map

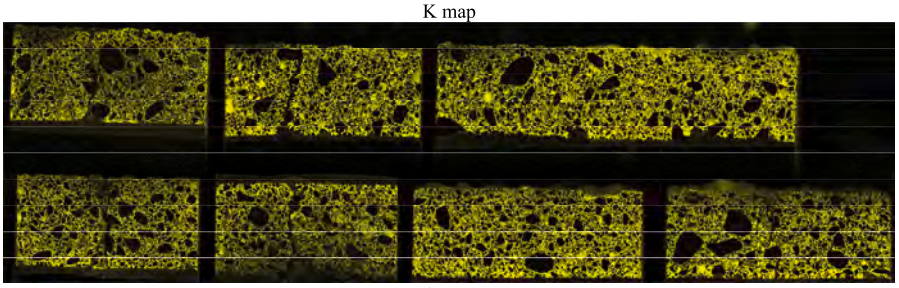

S map

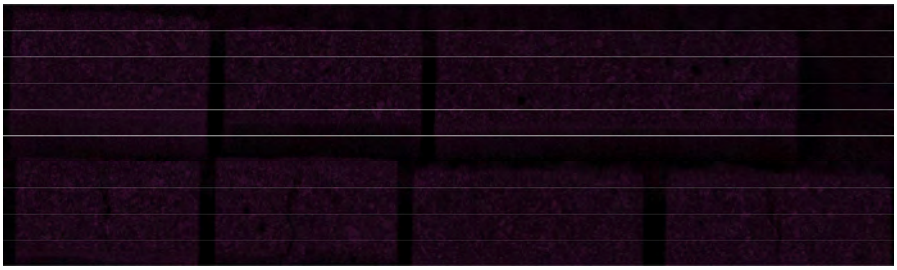

Na map

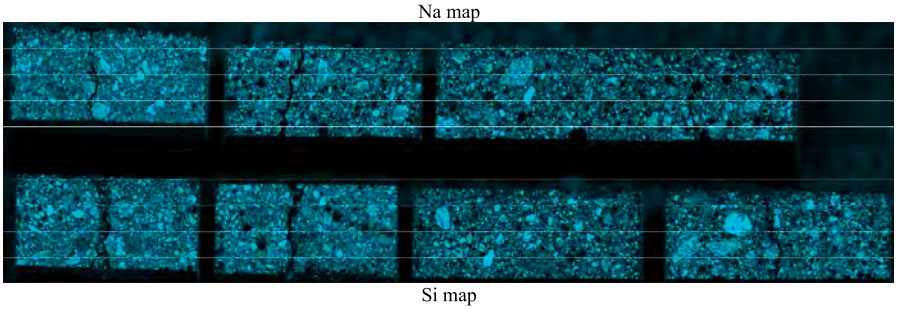

Si map

Fig. A2. (*continued*).

CMN-ED-I Ke*	CMN-ED-I	CMN-ED-II	
ASW-ED-I Ke*	ASW-ED-I	ASW-ED-II	ASW-ED-III
Ke*: Specimens cut using Kerosene			

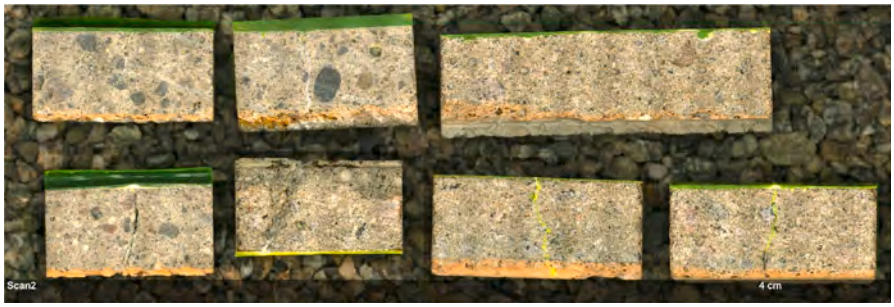

Mosaic

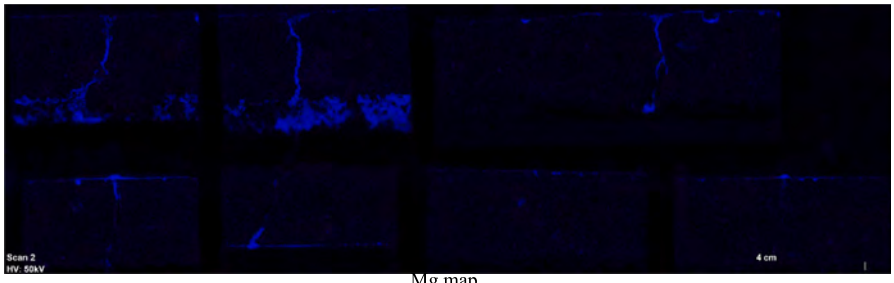

Mg map

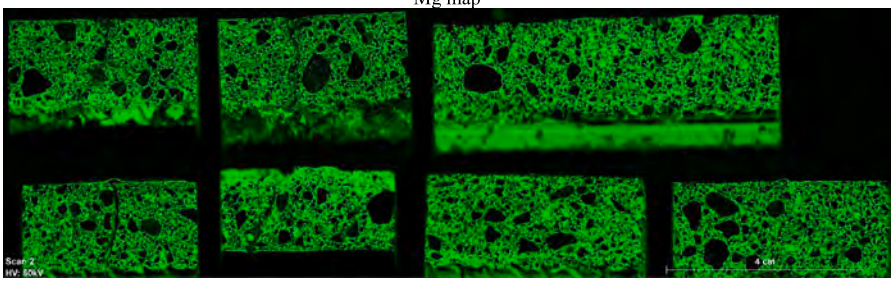

Ca map

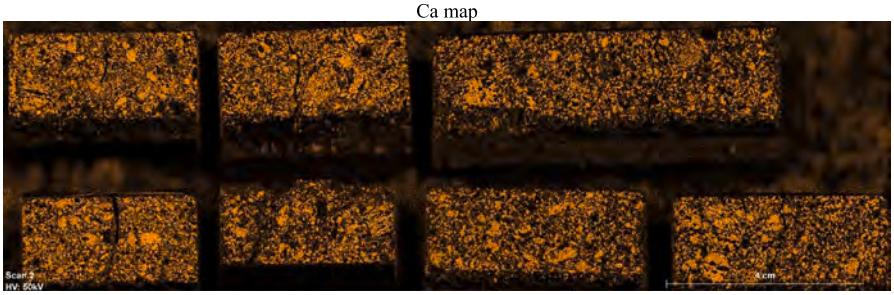

Al map

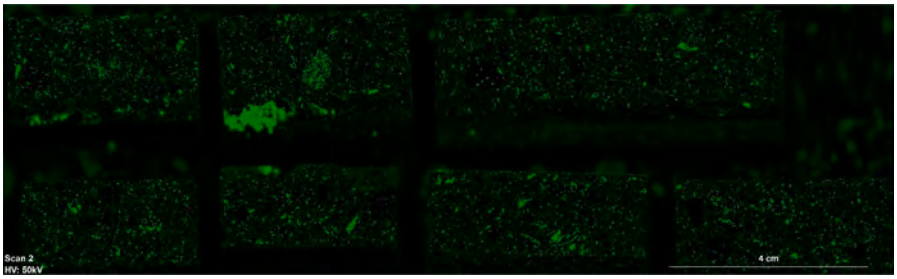

Fe map

Fig. A3. Elemental mapping of electrodeposited specimens (Scan 2).

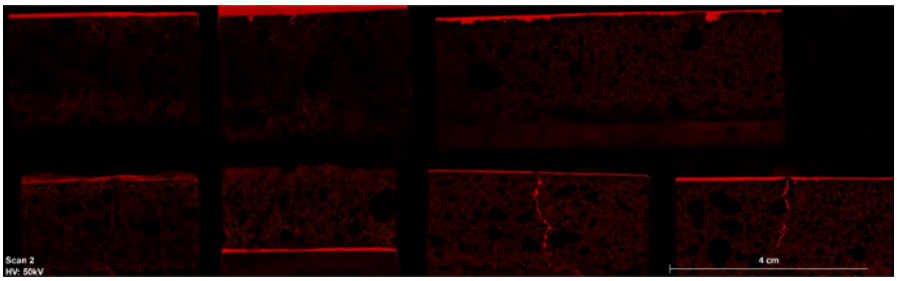

Cl map

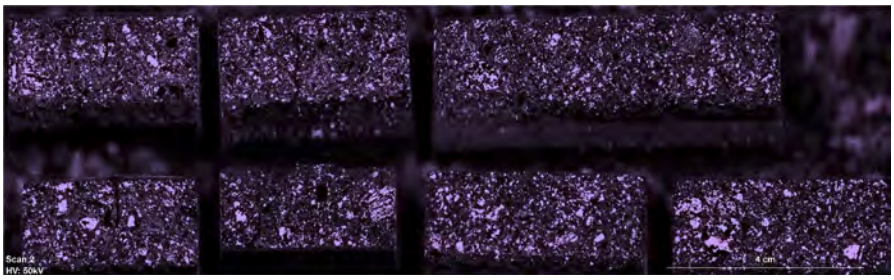

K map

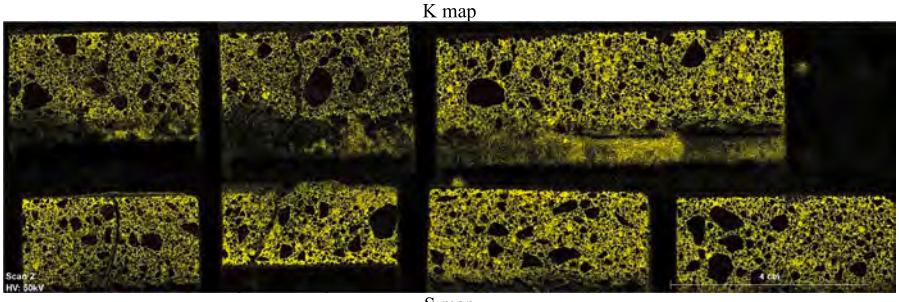

S map

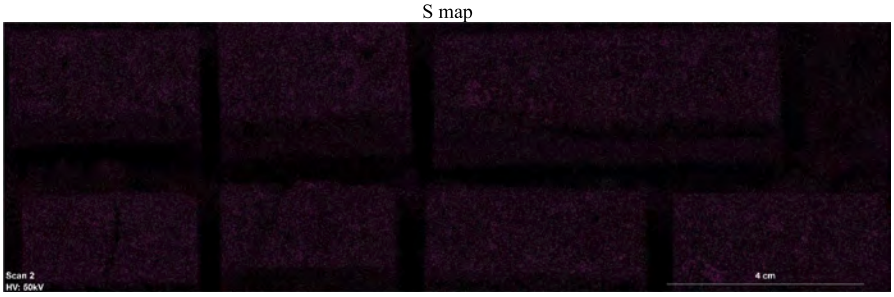

Na map

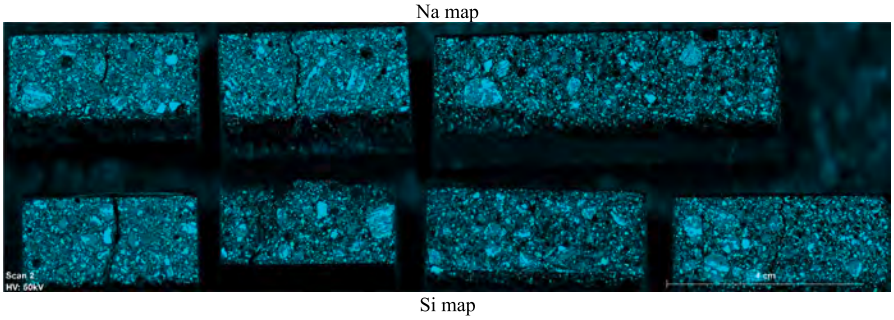

Si map

Fig. A3. (*continued*).

Data availability

Data will be made available on request.

References

[1] S. Robuschi, O.L. Ivanov, M. Geiker, I. Fernandez, K. Lundgren, Impact of cracks on distribution of chloride-induced reinforcement corrosion, Mater. Struct. 56 (2022) 7, https://doi.org/10.1617/s11527-022-02085-6.

[2] U.M. Angst, M.R. Geiker, M.C. Alonso, R. Polder, O.B. Isgor, B. Elsener, H. Wong, A. Michel, K. Hornbostel, C. Gehlen, R. François, M. Sanchez, M. Criado, H. Sørensen, C. Hansson, R. Pillai, S. Mundra, J. Gulikers, M. Raupach, J. Pacheco, A. Sagüés, The effect of the steel–concrete interface on chloride-induced corrosion initiation in concrete: a critical review by RILEM TC 262-SCI, Mater. Struct. 52 (2019) 88, https://doi.org/10.1617/s11527-019-1387-0.

[3] E. Chen, C.G. Berrocal, I. Löfgren, K. Lundgren, Correlation between concrete cracks and corrosion characteristics of steel reinforcement in pre-cracked plain and fibre-reinforced concrete beams, Mater. Struct. 53 (2020) 33, https://doi.org/10.1617/s11527-020-01466-z.

[4] U.M. Angst, M.R. Geiker, A. Michel, C. Gehlen, H. Wong, O.B. Isgor, B. Elsener, C. M. Hansson, R. François, K. Hornbostel, R. Polder, M.C. Alonso, M. Sanchez, M. J. Correia, M. Criado, A. Sagüés, N. Buenfeld, The steel–concrete interface, Mater. Struct. 50 (2017) 143, https://doi.org/10.1617/s11527-017-1010-1.
[5] S. Bano, G. Jaiswal, R. Kumar, A. Tiwari, M. Karthikeyan, Experimental study on the crack repair techniques of concrete structures: a case study, IOP Conf. Ser. Mater. Sci. Eng. 1273 (2023) 012006, https://doi.org/10.1088/1757-899X/1273/1/012006.
[6] N.-E. 1504-9:2008+NA:2013, Products and Systems for the Protection and Repair of Concrete Structures - Definitions, Requirements, Quality Control and Evaluation of Conformity - Part 9: General Principles for the Use of Products and Systems, Norway, 2013.
[7] L. Bertolini, B. Elsener, P. Pedeferri, E. Redaelli, R. Polder, Corrosion of Steel in Concrete: Prevention, Diagnosis, Repair, John Wiley & Sons, New York, USA, 2013, https://doi.org/10.1002/9783527651696.
[8] T. Danner, U. Hjorth Jakobsen, M.R. Geiker, Mineralogical sequence of self-healing products in cracked marine concrete, Minerals 9 (2019) 284, https://doi.org/10.3390/min9050284.
[9] W. Hilbertz, Mineral Accretion of Large Surface Structure, Building Components and Elements, 1981. United States of America.
[10] W. Hilbertz, Repair of Reinforced Concrete Structures by Mineral Accretion, 1984. United States of America.
[11] J.-S. Ryu, N. Otsuki, Crack closure of reinforced concrete by electrodeposition technique, Cement Concr. Res. 32 (2002) 159–164, https://doi.org/10.1016/S0008-8846(01)00650-0.
[12] T. Nishida, N. Otsuki, A. Saito, Development of improved electrodeposition method for repair of reinforced concrete structures, in: 4th International Conference on Durability of Concrete Structures, 2014, p. 10, https://doi.org/10.5703/1288284315428.
[13] H. Chu, L. Jiang, C. Xiong, L. You, N. Xu, Use of electrochemical method for repair of concrete cracks, Constr. Build. Mater. 73 (2014) 58–66, https://doi.org/10.1016/j.conbuildmat.2014.09.031.
[14] H. Chu, L. Jiang, Z. Song, Y. Xu, S. Zhao, C. Xiong, Repair of concrete crack by pulse electro-deposition technique, Constr. Build. Mater. 148 (2017) 241–248, https://doi.org/10.1016/j.conbuildmat.2017.05.033.
[15] D. Shirole, G. Volpatti, A. Guerini, D. Zampini, G. Cusatis, A.F. Rotta Loria, Effects of electrodeposition in concrete mediated by electric currents of variable polarity, Cement Concr. Res. 172 (2023) 107254, https://doi.org/10.1016/j.cemconres.2023.107254.
[16] Z. Qian, Q. Chen, H. Yang, A review on electrodeposition repair of cracked reinforced concrete, in: F. Biondini, D.M. Frangopol (Eds.), Life-Cycle of Structures and Infrastructure Systems, CRC Press, London, 2023, pp. 4043–4050, https://doi.org/10.1201/9781003323020.
[17] Q. Chen, L. Xie, H. Zhu, W. Liu, Z. Jiang, Z. Zhang, D. Zhang, B. Li, J.-W. Woody Ju, Insight into ettringite induced concrete crack healing by electrodeposition: effects of electrochemical parameters and numerical simulations, Cem. Concr. Compos. 149 (2024) 105504, https://doi.org/10.1016/j.cemconcomp.2024.105504.
[18] N. Otsuki, J.-S. Ryu, Use of electrodeposition for repair of concrete with shrinkage cracks, J. Mater. Civ. Eng. 13 (2001) 136–142, https://doi.org/10.1061/(ASCE)0899-1561(2001)13:2(136).
[19] J. Xu, W. Feng, H. Shan, L. Jiang, L. Tang, Application of electrodeposition method in upgrading mortar durability, J. Adv. Concr. Technol. 13 (2015) 367–372, https://doi.org/10.3151/jact.13.367.
[20] H. Chu, L. Jiang, N. Xu, C. Xiong, Influence of anion types on the electrodeposition healing effect of concrete cracks, J. Wuhan Univ. Technol.-Materials Sci. Ed. 27 (2012) 1154–1159, https://doi.org/10.1007/s11595-012-0621-1.
[21] T.N.N. Shin, H. Minagawa, W. Yodsudjai, Investigation of the durability of land-based reinforced concrete members after electrodeposition repair, Zairyo 51 (2002) 1278–1283, https://doi.org/10.2472/jsms.51.1278.
[22] K. De Weerdt, B. Lothenbach, M. Geiker, Comparing chloride ingress from seawater and NaCl solution in Portland cement mortar, Cement Concr. Res. 115 (2019) 80–89, https://doi.org/10.1016/j.cemconres.2018.09.014.
[23] S. Robuschi, A. Tengattini, J. Dijkstra, I. Fernandez, K. Lundgren, A closer look at corrosion of steel reinforcement bars in concrete using 3D neutron and X-ray computed tomography, Cement Concr. Res. 144 (2021) 106439, https://doi.org/10.1016/j.cemconres.2021.106439.
[24] E. Rossi, R. Polder, O. Copuroglu, T. Nijland, B. Šavija, The influence of defects at the steel/concrete interface for chloride-induced pitting corrosion of naturally-deteriorated 20-years-old specimens studied through X-ray computed tomography, Constr. Build. Mater. 235 (2020) 117474, https://doi.org/10.1016/j.conbuildmat.2019.117474.
[25] J. Taheri-Shakib, A. Al-Mayah, Dynamics of localized accelerated corrosion in reinforced concrete: Voids, corrosion products, and crack formation, Ceram. Int. 50 (2024) 48755–48767, https://doi.org/10.1016/j.ceramint.2024.09.229.
[26] Dragonfly software (academic license), Version 2024.1.0.1627 [Windows], Object Research Systems (ORS), Inc., Montreal, Canada, 2024. http://www.theobjects.com/dragonfly.
[27] J.S. Ryu, Influence of crack width, cover depth, water-cement ratio and temperature on the formation of electrodeposits on the concrete surface, Mag. Concr. Res. 55 (2003) 35–40, https://doi.org/10.1680/macr.2003.55.1.35.
[28] J.S. Ryou, N. Otsuki, Experimental study on repair of concrete structural members by electrochemical method, Scr. Mater. 52 (2005) 1123–1127, https://doi.org/10.1016/j.scriptamat.2005.02.001.
[29] L. Bertolini, B. Elsener, P. Pedeferri, E. Redaelli, R. Polder, Inspection and condition assessment, in: Corrosion of Steel in Concrete: Prevention, Diagnosis, Repair, John Wiley & Sons, New York, USA, 2013, https://doi.org/10.1002/9783527651696.